Towards a Predictive, Physics-Based Friction Model for the Dynamics of Jointed Structures

Justin H. Porter *[1] and Matthew R. W. Brake †[1]

[1]Department of Mechanical Engineering, Rice University, Houston, TX 77005

January 20, 2023

Abstract

Bolted connections are ubiquitous in mechanical designs and pose a significant challenge to understanding and predicting the vibration response of assembled structures. The present paper develops a physics-based rough contact model of the frictional interactions within a joint. This model sums over the probable interactions of asperities - defined as locally maximum surface features - to determine the contact forces. Here, the tangential contact forces vary smoothly between sticking and slipping and allow the model to better capture the qualitative trends of experimental amplitude dependent frequency and damping than previous studies. Furthermore, the novel model is generalized to allow for arbitrarily varying normal pressure including potential separation to better represent the interfacial dynamics. This includes developing a new, computationally tractable approximation to the analytical Mindlin partial slip solution for tangential loading of contacting spheres. The results highlight the importance of accurately characterizing the as-built topology of the interface, the plastic behavior of the contacting asperities, the relevant length scale of asperities, and the eccentricity of asperities. A predictive friction coefficient based on plasticity provides a poor match to experiments, so fitting the friction coefficient is also considered. Numerical results are compared to experiments on the Brake-Reuß Beam to assess the predictive potential of the models. While blind predictions over-predict the slip limit, the current model presents a significant improvement in physics-based modeling and highlights areas for ongoing research.

Keywords— Jointed Structures; Rough Contact; Frictional systems; Microslip; Hysteretic systems; Zero-Thickness Elements

---

*jp88@rice.edu

†brake@rice.edu

1 Introduction

The dynamic behavior of bolted joints, used throughout mechanical engineering, is increasingly important as assemblies and engines are optimized to improve efficiency [1]. Traditional approaches over-designed jointed connections to prevent failure, resulting in excessive weight. Efforts to reduce the weight due to over-design require accurate models to understand the behavior of the jointed connections. Recent efforts have decreased the error in the calculation of low amplitude frequencies [2, 3]. However, these models still struggle to predict the nonlinear amplitude dependent frequency and damping. As an alternative, friction model parameters are frequently obtained by fitting models to match experimental data [4–7], but these model parameters are not generally applicable to other structures. While computationally efficient empirical models can be fit to experimental data and then applied to efficiently simulate structures, these approaches rely on significant amounts of experimental data [4–7]. However, sufficient experimental data is not always available, especially early in the design process before a prototype has been built. Predictive models have the potential to significantly improve early designs before costly prototypes are manufactured. While predictive models are not yet mature enough for general use, these models have the potential to reduce vibration testing costs significantly even if they are more computationally intensive than empirical models [1]. Highlighting the difficulties of blind predictions, developing predictions for a novel structure is the subject of a current challenge within the community [8].

Rough contact modeling provides a potential avenue for the development of predictive models based on measured surface parameters [9, 10]. Such models calculate the interactions between asperities - defined here as locally maximum surface features - of different heights, then integrate over a probability distribution describing the asperity heights to compute the expected contact forces. Several studies have extended rough contact modeling to include tangential interactions between asperities to either predict the tangential stiffness [2, 3] or to create microslip models, which have a smooth transition from fully stuck to slipping [11–13]. Outside of statistical approaches, some researchers have deterministically modeled asperity interactions with high resolution finite element models [14, 15]. However, such models are too computationally intensive and require too much detail from surface measurements for general use in industrial applications.

Predictive models based on rough contact can be divided into two categories: stick-slip models and microslip models. For stick-slip elements (e.g., a Jenkins element), the model consists of a linear tangential spring until a constant slip force is reached. The tangential stiffness and the normal behavior of these models can be obtained by applying the rough contact modeling approach to measured asperity statistics [2, 3]. Thus, they are able to be formulated in terms of material properties and a statistical description of the surface. However, these models used only elastic asperity interactions [2, 3] allowing for further improvement by incorporating plasticity. Alternatively, the tangential stiffness and slip limit may be obtained through fretting experiments designed to match the experimental conditions of the structure [16, 17]. These simple models are generalized easily to arbitrary loading histories and have long been used to model frictional contact [18]. However, a recent assessment of the model form error of different friction models suggests that these simple models are unable to capture experimental behavior adequately even for optimal (model fit) parameters [7]. Conversely, microslip models, which must be numerically fit to data, are suited to capture experimental behavior of structures better than the simple models [7, 19].

To create microslip tangential friction models, the rough contact modeling framework is applied to both the initial stiffness and the slip behavior of each asperity in the statistical representation of the surface [11, 12]. Here, the Cattaneo-Mindlin stiffness [20, 21], with a sudden transition to slipping, or the Mindlin partial slip solution [21–23] can be used for each asperity in the integral. Such models have shown promise in matching experimental data at a constant normal pressure [12, 24], but existing literature makes several simplifying assumptions [12, 25–29].

The primary simplification in many studies is to use a single frictional element for the full contact area and thus neglect spatial variations in contact pressure [12, 25–29], which neglects the kinematics of many jointed structures [30]. Adding to the modeling error, the experiments in [12] relied upon a torque driver to prescribe bolt torques, resulting in significant uncertainty in the preload value of the bolts (see [31] for a discussion of the variability in the relationship between bolt torque and preload). Similarly, later studies comparing to the same experimental data are limited by this experimental error [25, 26, 28, 29].

Most of the microslip models have only been applied using a constant normal pressure throughout the cycle [6, 12, 25–29]. These models only considered monotonic loading [27] or used the Masing hypotheses to generate full hysteresis loops [25, 26, 28, 29]. Therefore, these models are not generally applicable to real structures where the normal pressure varies and the Masing assumptions do not hold [7]. Additionally, many studies restrict their investigations to Gaussian distributions of asperity heights [12, 26, 28] while other studies have highlighted significant deviations in behavior for non-Gaussian surfaces [25, 27, 29, 32].

For rough contact models, there is significant uncertainty regarding how to best choose a friction coefficient [2, 3]. To make blind predictions of the frictional forces between contacting rough surfaces, several plasticity based friction coefficients have been proposed [12, 24, 33]. Such models offer a significant benefit since they do not require experimental data to fit the friction coefficient. These plasticity based friction coefficients have been applied with limited success to hysteresis loops in several studies [12, 24, 25]. However, previous studies did not consider dynamic testing of real joints, thus the present work tests the applicability of one of these plasticity based friction coefficients to real structures.

The present paper develops an approximate representation to the Mindlin partial slip solution that allows for general loading cases without simplifying the effects of variable normal pressure or arbitrary load reversal points. Both spherical and ellipsoidal asperities are considered since several studies have highlighted the importance of considering the ellipticity of the contacting asperities [34–37]. This model is then applied to an experimental benchmark to investigate the predictive potential of the model. Such an application is only possible since the model is generalized to allow for arbitrary loading histories and thus presents a novel description and application of microslip rough contact models. To capture the normal pressure accurately, recent experiments have measured bolt preloads [3, 38] and the present model uses a mesh capable of capturing the kinematics of the interface. Asperities are considered with both elastic and elastic-plastic behavior. In addition, friction coefficients are obtained both by fitting results to experimental data and using a plasticity based friction coefficient [12, 24] for a fully predictive model.

The rest of the paper is organized as follows. First, the new frictional contact model is developed in Section 2 to incorporate both arbitrary normal and tangential displacement histories and smooth tangential force-displacement relationships. This section includes details about elastic and plastic normal contact of asperities (see Section 2.1) so that the effect of including plasticity in the rough contact model can be investigated in the context of the benchmark jointed structure for the first time. In addition, two new approximations of the Mindlin partial slip solution are presented that allow for arbitrary normal and tangential displacement histories to investigate the importance of capturing microslip behavior at the asperity level (see Section 2.2). Then the system of interest and an improved method of identifying the surface parameters is described in Section 3. The nonlinear solution methods are described in Section 4. This is followed by the results of the modeling effort in Section 5 that provide new insights into the necessary physics for rough contact modeling for dynamic simulations of bolted connections. Finally, the main conclusions are summarized in Section 6.

2 Contact Models

The focus of the present paper is the frictional contact model between two surfaces. This section describes the equations for the friction model that are implemented into the numerical simulations conducted in Section 5. Here, two rough surfaces are idealized as being covered by a set of ellipsoidal asperities with constant radii. The geometry of the asperities is characterized by the two principal radii of curvature at the highest point. The heights of the asperities are characterized by a deterministic mesoscale topology that varies between elements and a statistical gap probability distribution function (PDF) that is constant across all elements. All of these asperity properties are calculated from surface scans as described in Section 3.2. Given the asperity properties, the frictional traction for a set of prescribed displacements can be calculated as described in this section and summarized in Figure 1. The asperities are assumed to start initially aligned between the two surfaces with all contact forces being transmitted by sets of asperities in contact.[1] The key feature of the rough contact model is that it provides a smooth transition from sticking to slipping (microslip) due to both asperities sliding at different tangential displacements and the microslip nature of the Mindlin-Iwan asperity models. Additionally, the model considers arbitrarily varying normal displacements with the potential for separation of the surfaces.

The reduced order model described in Section 3 produces Zero-Thickness Elements (ZTEs) that represent the local contact state. Each ZTE within the system model has a set of displacements u_x, u_y, and u_n. It

---

[1] While this assumption may not be generally valid, it is common for rough contact modeling [9, 12] and vastly simplifies the calculation by reducing the required number of random variables to integrate over. Future work could consider the effects of misaligned asperities.

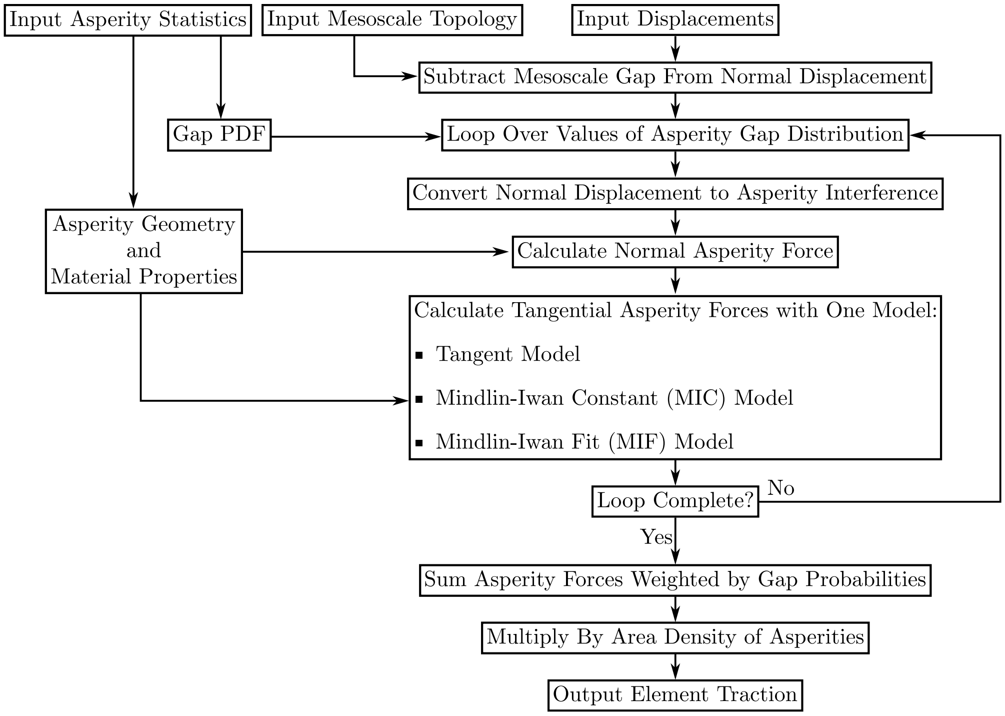

Figure 1: Overview of frictional force calculation.

is assumed that each asperity in the element displaces an equal amount (u_x, u_y, and u_n). However, the initial gap between asperities varies; for a set of asperity indexed i, the initial gap is z_i resulting in a normal interference of

$$\delta_i = u_n - z_i, \tag{1}$$

where $\delta_i = 0$ corresponds to the point of initial contact between the asperities. For an asperity area density of η, the total contact traction vector in an element, $\underset{\sim}{t}_{elem}$, is calculated as the numerical expectation of the traction on the element

$$\underset{\sim}{t}_{elem} = \eta \sum_{i=1}^{N_{asp}} p(z_i/z_{max}) \underset{\sim}{f}(u_x, u_y, \delta_i) w_i \tag{2}$$

for N_{asp} quadrature gaps in the element with initial values of z_i and weights w_i. The probability of an initial gap $p(z_i/z_{max})$ is calculated from the gap PDF[2] derived in Section 3.2. The asperity forces, $\underset{\sim}{f}$, are described throughout the following sections. For the present paper, the trapezoid rule[3] with $N_{asp} = 100$ equally spaced points is used for all models with $z_i \in [0, z_{max}]$, where z_{max} is the maximum gap between asperities on the two surfaces in the gap PDF.

---

[2] The gap PDF is derived as the probability distribution of the normalized gap, thus requiring the division by z_{max} here.

[3] The weights, w_i, are determined via the numerical integration scheme. For the trapezoid rule, the weights reduce to $w_1, w_{N_{asp}} = 1/[2(N_{asp} - 1)]$ and $w_i = 1/(N_{asp} - 1)\ \forall i \neq 1, N_{asp}$.

2.1 Normal Contact Models

The normal contact between asperities is divided into elastic loading, elastic-plastic loading, and elastic unloading regimes. The elastic loading is described by Hertz's contact model for both spherical and ellipsoidal contact geometries [39–41]. For spherical contact, the elastic-plastic regime is modeled with strain hardening [42], and the elastic unloading regime is modeled with a modified Hertzian contact law [43]. Here, ellipsoidal contact geometries are considered only for the fully elastic case. Some literature has investigated elastic-plastic ellipsoidal contacts [35–37, 44–46]; however, these models have not addressed unloading in the normal direction or the tangential stiffness of the contacting asperities, and thus cannot be applied in the current modeling effort. Furthermore, several of the models do not account for strain hardening in the plastic regime [36, 37, 44–46].

An overview of the different normal loading and unloading curves is shown in Figure 2. Here, the ellipsoidal asperities are slightly stiffer than spheres while the plastic model produces the lowest forces at a given displacement. After loading an asperity to a given force, the average stiffness on the unloading curve after plastic deformation is greater than that of the fully elastic contact model. Thus, introducing plastic deformation can result in a stiffer system for steady-state oscillations on the unloading curve.

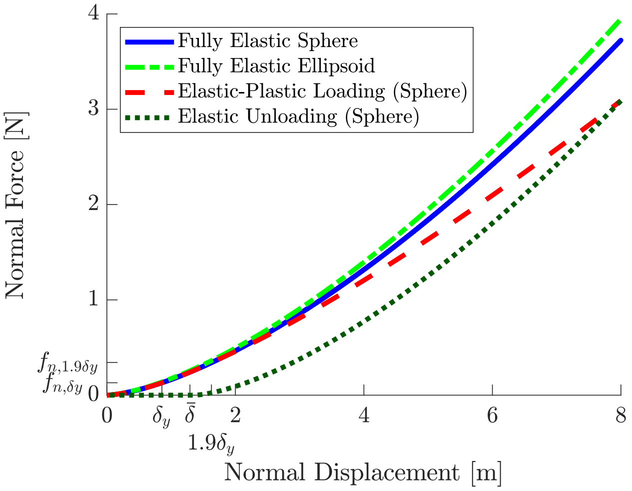

Figure 2: Overview of normal contact models.

2.1.1 Contact Parameters

Prior to calculating normal contact, several parameters must be defined. In Hertzian contact [39–41], each asperity is approximated as an elliptic paraboloid with large and small principal radii of R_i' and R_i'' respectively for an asperity indexed i (see Figure 3). For the present case, it is assumed that the principal radii of curvature are aligned between the two contacting asperities.[4] Therefore, the principal relative radii of

---

[4] This assumption greatly reduces the required computation time by eliminating an integral over possible orientations of each asperity and is consistent with assuming that asperities are aligned due to the machining process [34, 47].

curvature are defined as [40]

$$R' = \left(\frac{1}{R_1'} + \frac{1}{R_2'}\right)^{-1} \tag{3}$$

$$R'' = \left(\frac{1}{R_1''} + \frac{1}{R_2''}\right)^{-1}, \tag{4}$$

and an equivalent radius, R_e for the contacting asperities is defined as

$$R_e = \sqrt{R'R''}. \tag{5}$$

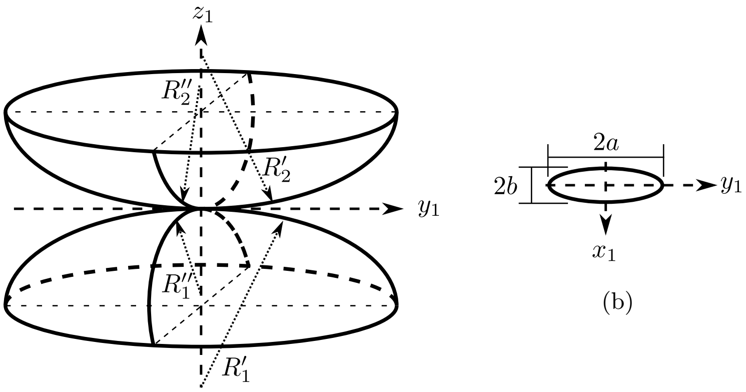

(b)

(a)

Figure 3: Schematic representation of ellipsoids in contact: (a) 3D view and (b) top view of contact area.

For ellipsoidal asperities, the ratio of the large, a, to the small, b, semi-axes of the contact ellipse, $\gamma = a/b$, is independent of the normal load.[5] Therefore, the value is found once numerically during initialization by solving the equation

$$\frac{\gamma^2 \boldsymbol{E}(e) - \boldsymbol{K}(e)}{\boldsymbol{K}(e) - \boldsymbol{E}(e)} - \frac{R'}{R''} = 0 \tag{6}$$

for the single variable γ where the eccentricity, e, of the contact area is

$$e = \sqrt{1 - 1/\gamma^2} \tag{7}$$

and $\boldsymbol{K}(e)$ and $\boldsymbol{E}(e)$ are the complete elliptic integrals of the first and second kind respectively.[6] During contact for the present case of aligned asperities, the large and small semi-axes of the contact area are aligned with the large and small principal radii of the asperities. For the case of spherical contacts, $\gamma = 1$ and $e = 0$.

2.1.2 Elastic Loading

For elastic loading, the normal force $f_{n,el}$ is [39, 40]

$$f_{n,el} = \frac{4E^*\sqrt{R_e}}{3[\boldsymbol{F_2}(e)]^{3/2}}\delta^{3/2}, \tag{8}$$

---

[5] The exact values of a and b vary with the normal load, but knowing the constant ratio γ simplifies the calculation at subsequent steps (see Section 2.1.2).

[6] Note that some numerical packages (e.g., MATLAB's `ellipke`) parameterize the elliptic integrals in terms of e^2.

where the subscript index on δ is dropped since only a single set of asperities is considered in this section. Here, E^* is the combined elastic modulus of the two asperities

$$E^* = \left(\frac{1-\nu_1^2}{E_1} + \frac{1-\nu_2^2}{E_2} \right)^{-1} \tag{9}$$

for asperities indexed i with elastic moduli E_i and Poisson's ratio ν_i. For the present study $E_1 = E_2 = E$ and $\nu_1 = \nu_2 = \nu$ yielding

$$E^* = \frac{E}{2(1-\nu^2)}. \tag{10}$$

In addition, two functions of the eccentricity of contact for normal loading are defined as [40]

$$\boldsymbol{F_1}(e) = \left[\frac{4}{\pi e^2} \right]^{1/3} (1/\gamma)^{1/2} \left[\{\gamma^2 \boldsymbol{E}(e) - \boldsymbol{K}(e)\}\{\boldsymbol{K}(e) - \boldsymbol{E}(e)\} \right]^{1/6} \tag{11}$$

and

$$\boldsymbol{F_2}(e) = \frac{2}{\pi} \left(\frac{1}{\gamma} \right)^{1/2} \frac{\boldsymbol{K}(e)}{\boldsymbol{F_1}(e)}. \tag{12}$$

For the case of spherical contacts, $\boldsymbol{F_1}(e) = \boldsymbol{F_2}(e) = 1$. The equivalent contact radius c is

$$c = \sqrt{ab} = \left[\frac{3 f_{n,el} R_e}{4E^*} \right]^{1/3} \boldsymbol{F_1}(e) \tag{13}$$

yielding principal contact radii

$$b = \frac{c}{\sqrt{\gamma}} \tag{14a}$$

$$a = b\gamma, \tag{14b}$$

where the ratio $\gamma = a/b$ is known from the initialization step (see Section 2.1.1). For the case of spherical asperities, the contact radius simplifies to

$$a = b = \sqrt{R_e \delta}. \tag{15}$$

2.1.3 Elastic-Plastic Loading

After the initiation of yield, the asperities are modeled as elastic-plastic spheres with strain hardening [42]. In the plastic regime, the local stiffness is described by a hardening modulus E_t. For the present model, the elastic-plastic sphere on an elastic flat model from [42] is converted to the case of symmetric loading of two elastic-plastic spheres representing the asperities. Due to symmetry, the contact of two identical spheres can be represented as a single sphere pressed against a rigid plane. Here, each sphere takes half of the displacement and has a radius of $2R_e$ (see Section 2.1.1). Furthermore, the effective elastic modulus of a single sphere and the rigid plane is $2E^*$. This section presents the modified equations from [42] with these assumptions such that E^*, R_e, and δ are defined identically as in the previous sections.

The critical deformation is determined via equating the von Mises stress from the Hertzian solution to the yield strength of the material [40, 43, 48]. The yielding occurs at a depth z or a nondimensional depth $\chi = z/a$ which solves [33, 49]

$$(1+\nu) \left[\tan^{-1}(1/\chi) - \frac{\chi}{1+\chi^2} \right] - \frac{3\chi}{(1+\chi^2)^2} = 0 \tag{16}$$

for a given Poisson's ratio ν. This equation is approximated in [42, 50] via a best fit to the numerical solutions as a function of ν giving a ratio of maximum contact pressure to yield strength of

$$C = 1.295e^{0.736\nu}. \tag{17}$$

When the approximation of [42, 50] is substituted into the force-displacement equation for Hertzian contact, the critical displacement[7] for the inception of yield is found

$$\delta_y = \left(\frac{\pi C S_{ys}}{2E^*}\right)^2 R_e, \tag{18}$$

where S_{ys} is the yield strength of the asperity. Once the normal displacement exceeds the transition to the elastic-plastic regime of $1.9\delta_y$ as defined by [42] (see Figure 2), all subsequent calculations use the elastic-plastic loading model or the elastic unloading model (see Section 2.1.4).

Next, the elastic contact radius is calculated with (15) and the plastic radius is calculated as [42]

$$a_p = 2R_e\left(\frac{\pi C S_{ys}}{4E^*}\right)\sqrt{\frac{\delta}{\delta_y}\left(\frac{\delta}{1.9\delta_y}\right)^B} \tag{19}$$

for exponent

$$B = 0.14e^{\frac{23S_{ys}}{2E^*}}, \tag{20}$$

which is found from a best fit curve of high fidelity simulations considering a range of material properties. To interpolate between the contact radii, the parameter Υ is introduced [42][8]

$$\Upsilon = -2\sqrt{\frac{E}{S_{ys}}}\left(\frac{E_t}{E}\right)^{1-\frac{\delta-\delta_y}{4R_e}}\left[\left(4-3e^{-2\frac{E_t}{E}\sqrt{\frac{E}{S_{ys}}}}\right)\left(1-\frac{E_t}{E}\right)\right]^{-1}, \tag{21}$$

where E_t is the strain hardening modulus of the asperities. The contact radius is taken as [42]

$$a = a_e + (a_p - a_e)e^{\Upsilon}. \tag{22}$$

This contact radius is used within the tangential asperity models where necessary for the elastic-plastic loading. Next, the force parameters are

$$\frac{H}{S_{ys}} = 2.84 - 0.92\left[1-\cos\left(\frac{\pi a}{2R_e}\right)\right] \tag{23a}$$

$$F_c = \frac{4}{3}\left[\frac{R_e}{E^*}\right]^2\left[\frac{C\pi S_{ys}}{2}\right]^3. \tag{23b}$$

The elastic contact force is calculated with (8) with $\boldsymbol{F_2}(e) = 1$ for the spherical case. The fully plastic contact force is calculated as [42]

$$f_{n,p} = F_c\left[e^{-0.25\left[\frac{\delta}{\delta_y}\right]^{5/12}}\left(\frac{\delta}{\delta_y}\right)^{3/2} + \frac{H}{S_{ys}}\frac{1}{C}\frac{\delta}{\delta_y}\left(1-e^{-\frac{1}{25}\left(\frac{\delta}{\delta_y}\right)^{5/9}}\right)\right] \tag{24}$$

Finally, the elastic-plastic force with strain hardening is calculated as [42]

$$f_{n,ep} = f_{n,p} + (f_{n,el} - f_{n,p})(1 - e^{-3.3E_t/E}) \tag{25}$$

based on interpolating between the plastic and elastic forces.

---

[7] This is the total displacement between two spheres in contact and thus twice that provided in [42].

[8] Note, there is a typo in [42] that is corrected here after consulting the authors.

2.1.4 Elastic Unloading

After a maximum normal displacement causes the contacting asperities to yield, subsequent normal contact with smaller normal displacements is treated by the elastic unloading regime. Several studies agree that unloading should be elastic [43, 51], but the exact form is not agreed upon. A common assumption is to treat the unloading as an elastic sphere with a modified radius of curvature and residual deformation [43, 51]. To ensure continuity of both the contact radius and force at the reversal point, the residual deformation and modified radius of curvature are uniquely defined as calculated in [51]. However, a better match can be achieved to experiments by allowing a discontinuity in the contact radius as done in [43]. Since the model in [43] is experimentally validated for the normal loading case, it is used here.

After a maximum loading force f_m and displacement δ_m, the residual deformation of the asperities (see Figure 2) is modeled as [43]

$$\bar{\delta} = \delta_m \left[1 - \frac{3F_m}{4E^* \sqrt{R} \left(\delta_m^{3/2} \right)} \right] \tag{26}$$

and the modified radius of curvature as

$$\bar{R}_e = \frac{F_m^2}{\left(\frac{4}{3} E^* \right)^2 (\delta_m - \bar{\delta})^3} \tag{27}$$

The contact force is then

$$f_{n,ul} = \frac{4}{3} E^* \sqrt{\bar{R}_e} \left(\delta - \bar{\delta} \right)^{3/2} \tag{28}$$

while $\delta \geq \bar{\delta}$ so that the asperities remain in contact. Finally, the tangential asperity models make use of the contact radius

$$a = \sqrt{\bar{R}_e (\delta - \bar{\delta})}. \tag{29}$$

It is important to emphasize that the contact radius in [43] is discontinuous when the normal displacement reverses from the maximum value. This can cause significant numerical convergence issues if the tangential asperity models are used with both the elastic-plastic and elastic unloading models. However, in the present work this issue does not come up. Furthermore, the choice of using a within the tangential models (see Section 2.2) is consistent with the assumption of elastic unloading of spheres in contact. However, this has not been experimentally validated or verified against high resolution FEM. Further development of contact mechanics models has the potential to improve the asperity contact equations and thus the model in the present work.

2.2 Tangential Contact Models

The tangential stiffness K_t^q of identical spherical or elliptical contacts derived from elasticity without slipping at the contact[9] is [20, 21, 52]

$$K_t^q = \frac{4Ga}{(2 - \nu)\Phi_q} \tag{30}$$

---

[9] These solutions use Hertzian normal contact [39–41].

for material shear modulus G, large semi-axis of contact a, and correction factor Φ_q defined for loading aligned with the q semi-axis (either a or b) as

$$\Phi_a = \frac{4}{\pi(2-\nu)}\left[\left(1-\nu+\frac{\nu}{e^2}\right)\boldsymbol{K}(e) - \frac{\nu\boldsymbol{E}(e)}{e^2}\right] \tag{31}$$

and

$$\Phi_b = \frac{4}{\pi(2-\nu)}\left[\left(1-\frac{\nu}{e^2}\right)\boldsymbol{K}(e) + \frac{\nu\boldsymbol{E}(e)}{e^2}\right]. \tag{32}$$

Here, the superscript q on K_t^q indicates that the stiffness is different depending on the orientation of the loading except for the case of spheres where $\Phi_a = \Phi_b = 1$. The following sections describe how this tangential stiffness is incorporated into either a single slider for the tangent model or numerous sliders for the novel Mindlin-Iwan models (schematically shown in Figure 4). In addition, each of the models uses a friction coefficient μ either chosen to match experimental data or based on plasticity as described in Section 2.3.

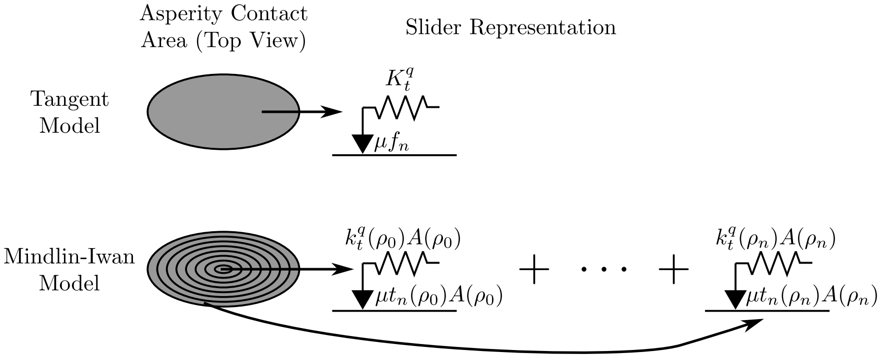

Figure 4: Schematic representation of the discretization of the contact area for the different tangential asperity models. For the Mindlin-Iwan Models, A represents the contact area associated with each slider and ρ_i represents the reference radius of each slider as defined by the integration scheme (e.g., see (38)). The full definition of variables and equations describing frictional forces are presented in Section 2.2.1 and Section 2.2.2 for the tangent and Mindlin-Iwan models respectively.

2.2.1 Tangent Asperity Model

The tangent model is the simplest considered asperity model and uses the tangential stiffness of (30) for a stick-slip element, referred to here as elastic dry friction. Here, elastic dry friction is used at the asperity level compared to previous applications at the macroscale level [2, 7, 18]. For a loading direction q, the force $f_{t,tan}$ for a current tangential displacement of u_t^q given a previous force and displacement state of $f_{t,0}^q$ and $u_{t,0}^q$ is [2, 7]

$$f_{t,tan} = \begin{cases} \underbrace{K_t^q(u_t^q - u_{t,0}^q) + f_{t,0}^q}_{f_{t,stuck}} & |f_{t,stuck}| < \mu f_n \\ \mu f_n \ \mathrm{sgn}(f_{t,stuck}) & \mathit{Otherwise} \end{cases} . \tag{33}$$

Here, μ is a coefficient of friction (see Section 2.3) and f_n is the current normal force from Section 2.1. If the asperity was out of contact at the previous step (i.e., $\delta < 0$), then $u_{t,0}$ is estimated with linear interpolation between the normal and tangential displacements as the tangential displacement where normal contact is re-established for the quasi-static solution method (see Section 4.2) [7]. For the frequency domain solutions (see Section 4.3), the force is calculated at more frequent intervals throughout the cycle and thus uses $u_{t,0}$ as the displacement at the previous step to limit the complexity of the gradient calculations. When summing over sufficient asperities with (2), the tangent model produces qualitatively smooth hysteresis loops despite the stick-slip behavior at the asperity level.

2.2.2 Mindlin-Iwan Constant Asperity Model

The Mindlin partial slip solution uses elasticity to describe the behavior of spheres [21–23] or ellipsoids [52] in contact and subject to tangential forces using a local Coulomb friction coefficient and the normal traction distribution from Hertzian contact to define a limit on the tangential tractions. To capture this behavior more accurately, the contact region between the asperities is represented with concentric rings each represented as a different slider similar to the conceptual discretization of [53] for oblique contacts (see Figure 4). These sliders are chosen to have equal stiffness in the traction formulation giving rise to the Mindlin-Iwan Constant (MIC) model and are described by the new equations (36) and (38). Here, each slider uses an independent elastic dry friction model, allowing the model to capture microslip behavior while applying a simple friction law that can easily be generalized to arbitrary loading histories. The contact area is first mapped onto a reference unit circle with a new position ρ

$$\rho^2 = \left[\frac{x_1}{b}\right]^2 + \left[\frac{y_1}{a}\right]^2, \tag{34}$$

where x_1 and y_1 are local coordinates aligned with the semi-axes b (short) and a (long) respectively and with the origin at the center of the contact area. On the reference unit circle, the normal traction is [40]

$$t_n(\rho) = \frac{3f_n}{2\pi ab}\sqrt{1-\rho^2}. \tag{35}$$

The tangential stiffness is assumed to be spatially distributed over the full contact area yielding a traction tangential stiffness k_t^q of

$$k_t^q = \frac{K_t^q}{\pi ab}. \tag{36}$$

Then, the elastic dry friction contact model formulated in terms of tractions [2, 7] is applied to each ring representing a portion of the asperity contact area. The tangential traction t_t^q at a given radius of contact ρ in direction q is [2, 7]

$$t_t^q(\rho) = \begin{cases} \underbrace{k_t^q(u_t^q - u_{t,0}^q) + t_{t,0}^q}_{t_{t,stuck}^q} & |t_{t,stuck}^q| < \mu t_n \\ \mu t_n \ \mathrm{sgn}(t_{t,stuck}^q) & Otherwise \end{cases} \tag{37}$$

for current displacements u_t^q and previous displacement and traction $u_{t,0}^q$ and $t_{t,0}^q$ respectively. Here, it should be noted that $t_{t,0}^q$ will be evaluated at a different value of ρ from the previous step if the normal loading state changed to match the same physical radius of contact (linear interpolation is used). Furthermore, if the normal displacement has increased from the previous step, the area of new contact is assigned $t_{t,0} = 0$. All sliders in the Mindlin-Iwan models use the same previous tangential displacement $u_{t,0}$ as described in Section 2.2.1 even if new contact is established on the outer rings.

The tangential tractions are numerically integrated with equally spaced quadrature points ρ_i and associated weights w_i, calculated with the trapezoid rule, to yield a total tangential force of

$$f_{t,MIC} = 2\pi ab \sum_{i=1}^{N} w_i \rho_i t_t^q(\rho_i). \tag{38}$$

The trapezoid rule is used to provide a robust calculation of the force since the tractions are expected to have sharp discontinuities in slope between the stick and slip regions and to be consistent with the linear interpolation used to map the previous traction states $t_{t,0}^q$.

2.2.3 Mindlin-Iwan Fit Model

While the model in Section 2.2.2 recreates a smooth partial slip behavior, it has clear errors in matching the analytical partial slip solution at constant normal load (see Section 2.2.4). As an alternative, the tangential stiffness can be varied as a function of ρ to create the new Mindlin-Iwan Fit (MIF) model. To be generally applicable, a nondimensional form of the partial slip solution is fit where the nondimensional displacement $\tilde{u}_t$ is

$$\tilde{u}_t = \frac{2K_t^q}{3\mu f_n} u^q \tag{39}$$

and the nondimensional force $\tilde{f}_t$ is

$$\tilde{f}_t = \frac{f_t}{\mu f_n}, \tag{40}$$

resulting in a monotonic loading curve at constant normal load of [21–23, 52]

$$\tilde{f}_t = 1 - (1 - \tilde{u}_t)^{3/2}. \tag{41}$$

A new nondimensional tangential stiffness $\tilde{k}_t(\rho)$ of the form

$$\tilde{k}_t(\rho) = c_0 + \frac{1 - c_0}{\sqrt{1 - \rho^2}} + c_1\rho + c_2\rho^2 + c_3\rho^3 \tag{42}$$

is fit[10] to the analytical solution to obtain the coefficients c_0, c_1, c_2, and c_3 (given in Table 1). The parameter c_0 is limited to the domain $[0, 1]$ to ensure that the tangential stiffness at the center of contact results in

---

[10] The fit sought to minimize the maximum difference in force between the analytical monotonic loading curve at constant normal load before complete slip at 1000 equally spaced points and the force produced by the Iwan model as calculated with (38) and $N = 1000$ integration points. Note that only 100 integration points are used during the modeling of the structure to keep the calculations computationally feasible. More points are used in the fitting since it is only done a single time and to produce a fit that is a better approximation in the limit of a continuous integral.

slipping at the same displacement as full slip occurs in the analytical solution. The second term is chosen to approximate the behavior of the analytical solution for fully stuck contact[11] [21]. Finally the last three terms provide sufficient flexibility for the model to match the analytical solution. Furthermore, the fit parameters are checked to ensure that concentric rings slip in order from the outside to the inner most ring. While it is not possible to match the slip radii given in the full analytical solution exactly, this ensures that at least some of the physics is preserved. Since the fit is based on the non-dimensional representation, the values in Table 1 are valid for all subsequent analyses with this model.

The dimensional tangential stiffness at a given radius is then given by

$$k_t^q(\rho) = \frac{K_t^q}{\pi ab}\left[\tilde{k}_t(\rho)\right]. \tag{43}$$

The tractions on the contact area and the tangential force of the asperity are calculated with (37) and (38) respectively using this modified tangential stiffness.

Table 1: Parameters for fitting (42) to the analytical solution at constant normal load

Parameter	c_0	c_1	c_2	c_3
Value	0.8709	0.0629	-0.8915	0.6998

2.2.4 Comparison of Tangential Models

The goal for the Mindlin-Iwan models is to recreate the partial slip behavior for spheres or ellipsoids [21–23, 52]. Nondimensional comparisons, which are presented in Figure 5, are conducted by dividing the tangential displacement by the slip displacement $u_{t,slip}$ of

$$u_{t,slip} = \frac{3\mu f_n}{2K_t^q} \tag{44}$$

and dividing the tangential forces by μf_n.

Figure 5a shows a comparison between the three asperity models and the analytical solution for the case of constant normal load. In this case, the MIF model is indistinguishable from the analytical solution while the MIC model shows clear errors. Here, the tangent model provides an outer bounding box of the hysteresis loop without any microslip behavior. In Figure 5b, both Mindlin-Iwan models show decreasing tangential force while the normal load decreases compared to the analytical solution where the tangential force continues to increase. These errors can be attributed to the independent slider representation of the Mindlin-Iwan models being insufficient to capture the full tangential stiffness of the contact, which is fully coupled in the analytical elasticity solution. In Figure 5b, the transition in the normal force is nonlinear since the analytical solution provides a nonlinear stiffness for a fixed ratio of the rate of change of the normal

---

[11] Matching the analytical solution results in an infinite stiffness on the outer edge of contact. Numerically, this issue is avoided since the outer edge has zero normal traction and thus slips for any tangential displacement.

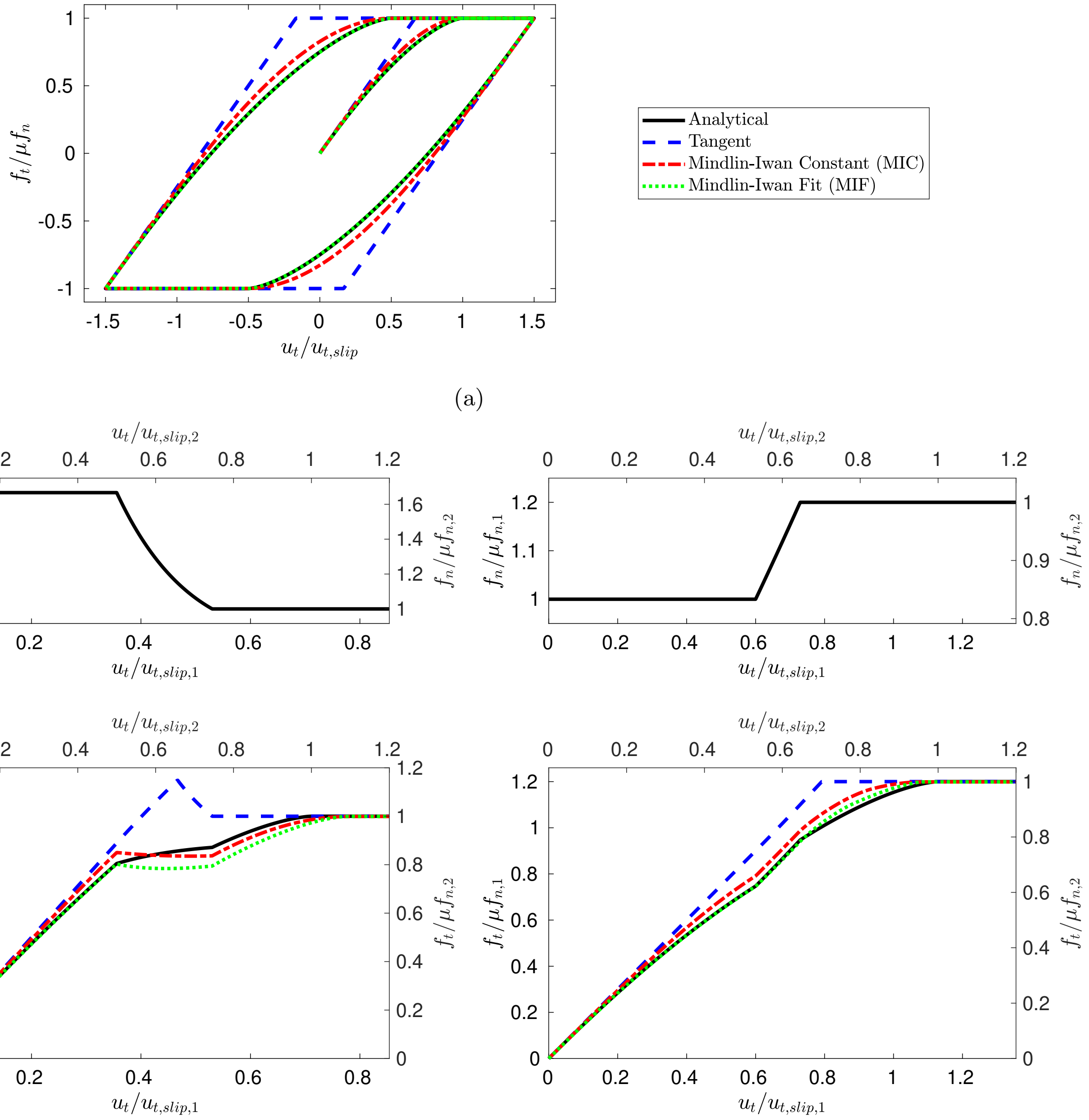

(a)

(b)

(c)

Figure 5: Example loading curves for asperity models compared to analytical solution [23] for (a) constant normal load, (b) a step down in normal load (at a rate of $df_n/df_t = -10/\mu$), and (c) a step up in normal load (at a rate of $df_n/df_t = 1/\mu$). The Mindlin-Iwan models both use 100 equally spaced quadrature radii and the trapezoid rule for integrating the tangential forces. The normal displacements and forces are exactly matched between all of the models and the analytical solution.

and tangential forces [23]. In this region, the analytical tangential displacement is calculated via numerical integration for the prescribed variation in the normal and tangential forces. Finally, for increasing normal load in Figure 5c, the MIF model accurately captures the transition because the asperity remains fully stuck, but then shows some error after the transition due to the inexact representation of the traction history and contact stiffness. While the cases for varying normal load show some errors in the Mindlin-Iwan models, these models still closely match the analytical behavior while providing a computationally tractable approach for arbitrary loading cases and histories. Furthermore, despite their errors, the Mindlin-Iwan models represent a clear improvement over the tangent model that only uses a single slider at the asperity level. For the present study, the three asperity models are used rather than the analytical solution since the analytical solution is not generally available for arbitrary loading histories (e.g., many reversal points at different tangential displacements with varying normal loads).

To understand the effect of the different models on the dynamics of a structure, the data presented in Figure 5a is transformed in Figure 6 to compare the secant stiffness and dissipation of the different models at constant normal load. The secant stiffness (see Figure 6a) affects the frequency of the response and the total displacements at the interface. Here, the tangent model over-predicts the stiffness by up to 24% and thus could be expected to result in higher frequencies than the other models. The MIC model also over-predicts the secant stiffness, but less severely than the tangent model, due to the assumed spatial distribution of tangential stiffness. Finally, the MIF model nearly exactly matches the secant stiffness of the analytical solution over a wide range of displacements. Both of the Mindlin-Iwan models under predict the secant stiffness near zero displacement due to the discretization of the models.

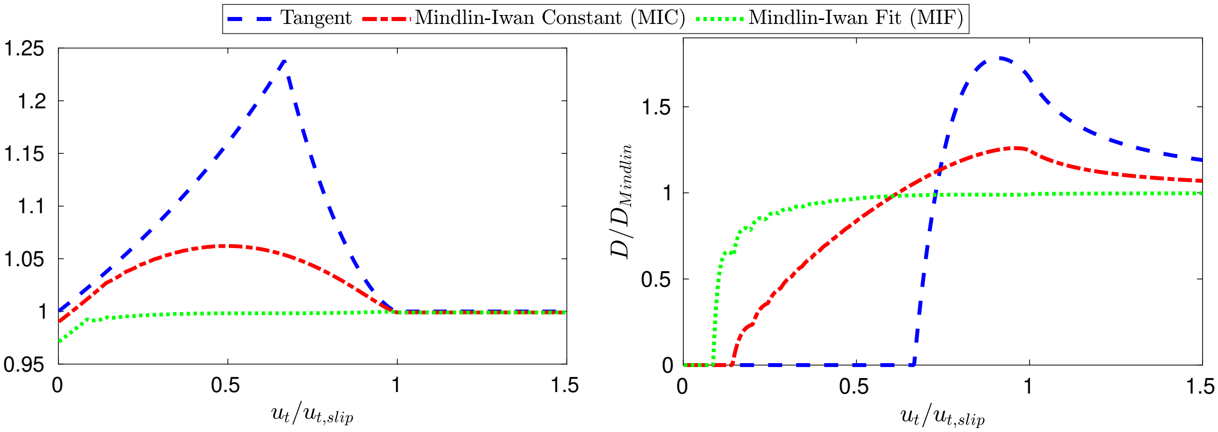

(a)

(b)

Figure 6: Comparison of (a) force values (equivalently secant stiffness) and (b) dissipation (oscillating between $\pm u_t$) of different asperity models to the analytical Mindlin solution at constant normal load. The Mindlin-Iwan models both use 100 equally spaced quadrature radii and the trapezoid rule for integrating the tangential forces.

In Figure 6b, all of the models initially under-predict the dissipation. The MIF model performs the best, rapidly rising to close to the analytical solution and then matching it. Alternatively, the tangent and MIC models both dissipate less energy than the Mindlin solution at small displacements then overshoot and dissipate more energy as they transition to macroslip. This suggests that depending on the loading regime, the tangent and MIC models could have significant errors in predictions of dissipation in comparison to the analytical solution. On the other hand, the MIF model appears to be a good match with minimal errors due to the discretization.

2.2.5 Coupling X and Y Directions

The previous asperity contact models have treated the frictional forces in the local a and b directions as independent. However, the slipping force in this approach is not invariant to the selected coordinate system. Alternatively, the traction relationships for each slider can couple the a and b directions resulting in a directionally invariant slip limit. This results in replacing (37) with the relationship [2, 7]

$$t_t^q(\rho) = \begin{cases} \underbrace{k_t^q(u_t^q - u_{t,0}^q) + t_{t,0}^q}_{t_{stuck}^q} & \sqrt{{t_{stuck}^a}^2 + {t_{stuck}^b}^2} < \mu t_n \\ \mu t_n \dfrac{t_{stuck}^q}{\sqrt{{t_{stuck}^a}^2 + {t_{stuck}^b}^2}} & Otherwise \end{cases}. \tag{45}$$

Here, t_{stuck}^a and t_{stuck}^b are used to determine a direction that the tangential traction acts while the second case applies the slip limit in that direction. For ellipsoidal asperities, the directionally invariant slip limit does not imply a directionally invariant friction model since the variable tangential stiffness results in slip being reached at different displacements for different loading directions.

2.3 Slip Limit

For all of the elastic asperity models and some of the plastic asperity models, a constant friction coefficient μ is chosen to match the experimental data. As an alternative, the CEB friction coefficient is considered to provide a slip limit without model fitting [24, 33]. The CEB friction coefficient defines the slipping force as the tangential force required to cause the inception of yield given the current normal loading condition. For the present model, it only makes sense to apply the CEB friction coefficient when plasticity is used for the normal contact of the asperities.

For the CEB model, the nondimensional normal displacement is calculated as

$$w^* = \frac{\delta - \bar{\delta}}{\delta_m - \bar{\delta}}. \tag{46}$$

For the case of purely elastic normal loading, $\bar{\delta} = 0$ and $\delta_m = 1.9\delta_y$ to be consistent with the normal contact model. The friction coefficient then is calculated as [24, 33]

$$\mu_{CEB} = \min\left[\frac{0.2045}{(0.454 + 0.41\nu)|c_1|}\sqrt{\frac{1}{w^*} - 1}\ ,\ \frac{-c_4 + \sqrt{c_4^2 - 4c_3c_5}}{2c_3}\right]. \tag{47}$$

The four[12] constants are [24, 33]

$$c_1 = -1 + \frac{3}{2}\chi \tan^{-1}\left(\frac{1}{\chi}\right) - \frac{\chi^2}{2(1+\chi^2)} \tag{48a}$$

---

[12] Numbering is chosen to be consistent with [24, 33], which define a constant c_2 before eliminating it in a simplification.

$$c_3 = \frac{9\pi^2}{16}\left(2 - \frac{\nu}{2} + \frac{7}{8}\nu^2\right) \tag{48b}$$

$$c_4 = \frac{9\pi}{4}(1-2\nu)\left(1 - \frac{\nu}{2}\right) \tag{48c}$$

$$c_5 = \frac{3}{2}(1-2\nu^2) - \frac{0.56}{(0.454+0.41\nu)^2 w^*}, \tag{48d}$$

and χ is the depth of the point of initial yielding nondimensionalized by the contact radius that is found from solving (16). For the present case of $\nu = 0.30$, $\chi = 0.48$ [24].

The CEB friction coefficient is based on the maximum tangential force to cause yielding in an elastic sphere at a given normal load. Since yielding of a single point does not correspond to complete plastic failure, the CEB model is generally expected to underpredict the friction coefficient if plastic deformation was the predominant cause of slipping. However, the model shows good agreement with some experiments [24], likely because other slip mechanisms are also involved. The present work extends prior applications of the CEB model to the dynamic behavior of a jointed structure to investigate the applicability of the model for new applications. Furthermore, the model is applied to an elastically unloading asperity after yielding as opposed to only considering monotonically increasing normal loading of the asperities as is done in previous studies [12].

2.3.1 Rotation of Orthotropic Friction

The tangential stiffness of the ellipsoidal contact models is orthotropic. Since the mesh directions may not align with the principal axes of the asperities, a rotation is implemented. For an asperity orientation α (measured counterclockwise from the positive x direction to the short semi-axis of the contact), the current displacements along the primary axes u_a, u_b (aligned with the long and short semi-axes a and b respectively) are

$$\begin{bmatrix} u_b \\ u_a \\ \delta \end{bmatrix} = \underbrace{\begin{bmatrix} \cos\alpha & \sin\alpha & 0 \\ -\sin\alpha & \cos\alpha & 0 \\ 0 & 0 & 1 \end{bmatrix}}_{Q} \begin{bmatrix} u_x \\ u_y \\ \delta \end{bmatrix}. \tag{49}$$

Forces on the transformed coordinate system, $\underset{\sim}{f}_{b,a,n}$, can be transformed back to the forces on the original coordinate system, $\underset{\sim}{f}_{x,y,n}$,

$$\underset{\sim}{f}_{x,y,n} = Q^T \underset{\sim}{f}_{b,a,n}. \tag{50}$$

3 System Model

3.1 System of Interest

The frictional contact model in Section 2 is applied to the Brake-Reuß Beam (BRB) to assess the predictive potential of the model. The BRB is a three bolt lap joint using bolts of nominal diameter 7.94 mm (5/16 inches); engineering drawings of the BRB can be found in [5]. Figure 7a shows the initial finite element model of the BRB from Abaqus. This model is then reduced in Abaqus with a Hurty/Craig Bampton Component Mode Synthesis [54, 55] to the interface degrees of freedom (DOFs) plus 19 fixed interface modes. The interface is remeshed using the procedure in [56] and previously applied in [7].[13] This produces a reduced order model (ROM) that has the interface representation shown in Figure 7b with 232 Zero-Thickness Elements (ZTEs), 846 nodal DOFs (3 directions × 282 Nodes) and 13 fixed interface modes.[14] The friction model is only evaluated at the 232 ZTEs and no solution steps require using the original interface mesh, resulting in a significant decrease in required computation time [56].

3.1.1 Experimental Measurements

Several measurements are conducted in order to provide both truth data to validate the new model against as well as the data necessary for model parameters (such as the elastic modulus and asperity properties). Prior to dynamic testing, both sides of the jointed interface are scanned as shown in Figure 7d. The details of the scanning and processing procedure are described in detail in Section 3.2. An average density of 7784.3 kg/m^3 is obtained by weighing the half beams and dividing by the nominal volume [3]. Free-free impact tests of the unassembled half beams are conducted to calculate the first natural frequency of each half beam and then an associated elastic modulus. The average elastic modulus of 192.31 GPa for the two half beams is used here [3]. Following the work of [3], a Poisson's ratio of 0.3 is used in the present work. The first set of simulations with plasticity use a yield strength of $S_{ys} = 330$ MPa and a hardening modulus of $E_t = 620$ MPa [57]. Second, a case with parameters of $S_{ys} = 150$ MPa and $E_t = 3.5$ GPa is considered [58].

The model is validated in Section 5 by comparing the predicted and measured nonlinear dynamics of the structure. For the assembled system, nonlinear behavior of the system with free-free boundary conditions is obtained via hammer impact testing [3, 38] using best practices from previous studies[15] [2, 59]. The response of the beam is recorded with an accelerometer near the end of the beam, and the beam is excited via hammer impact on the opposite side [3]. This data was filtered with a third order Butterworth bandpass filter[16] and then processed with the Peak-Finding and Fitting (PFF) method [60] to produce the nonlinear trends in frequency and damping shown in Figures 7c and 7e for the first and second bending modes respectively.

---

[13] MATLAB code from [56] is used for this procedure.

[14] Six rigid body modes are removed from the set of fixed interface modes as described in [2].

[15] The interface is aligned using an external guide and shims to ensure correct positioning of the bolt holes relative to both sides. Each bolt is torqued to approximately 70% of the desired tension starting with the middle bolt then the two outside bolts before all bolts were tightened to the desired tension in the same order. The exact tension values are measured with strain gauges on the bolts with the final average tension of the bolts being 12.249 kN.

[16] Center frequency of 178.5 Hz and a half-bandwidth of 7.5 Hz for the first bending mode and center frequency of 594.5 Hz and a half-bandwidth of 16.0 Hz for the second bending mode.

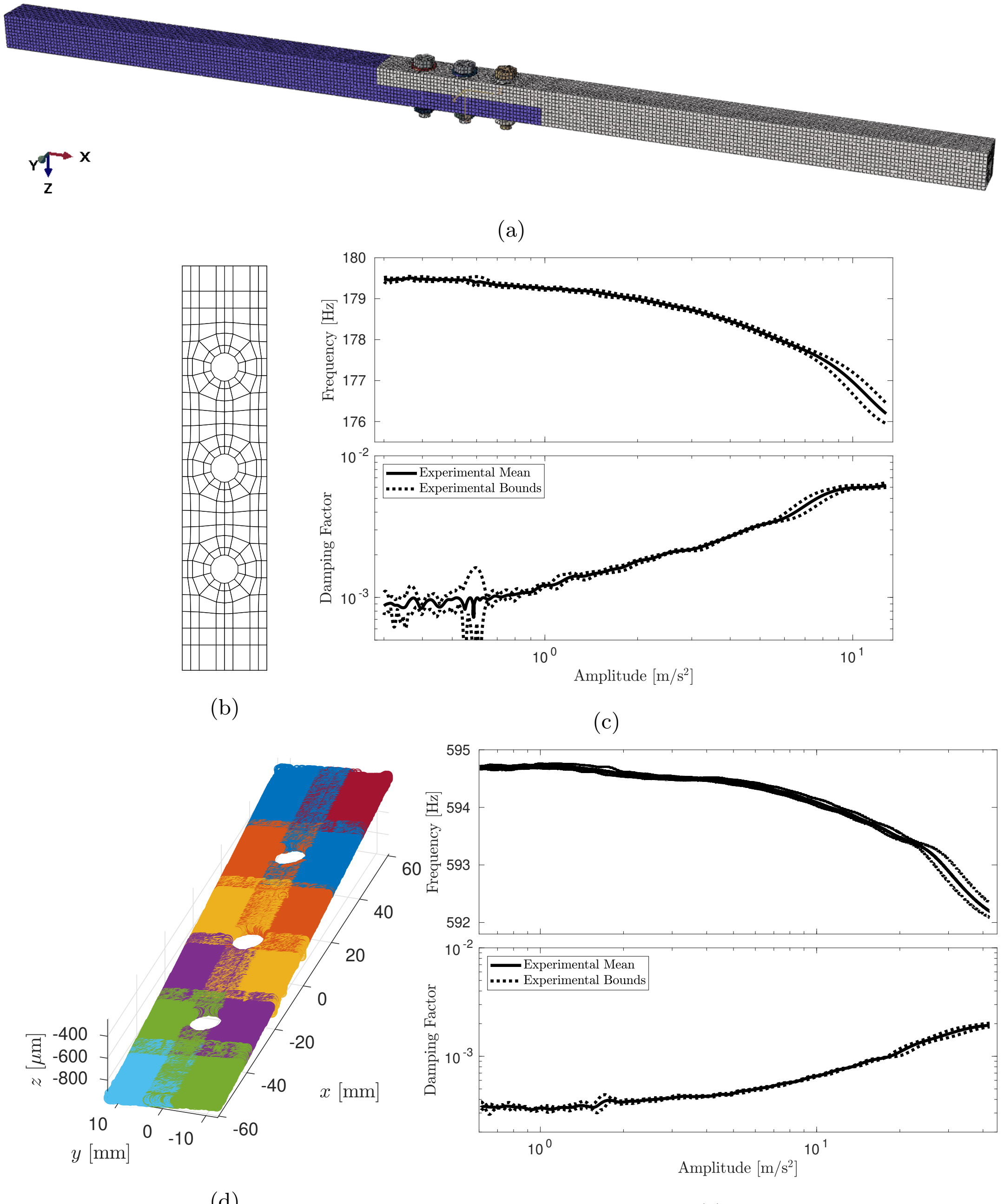

(a)

(b)

(c)

(d)

(e)

Figure 7: (a) Full BRB Model in Abaqus with the original mesh, (b) reduced interface mesh [56], (c) experimental trends in modal frequency and damping for the first bending mode, (d) example of raw interface scan data (each color indicates data from a different scan that has been stitched together to recreate the full interface), and (e) experimental trends in modal frequency and damping for the second bending mode.

3.1.2 Low Amplitude Damping

Determining the magnitude of material damping, even for linear structures, is an open challenge with significant uncertainty [61]. The present model considers only the frictional interactions of the interface and does not seek to predict the material damping. Previous experiments using a monolithic BRB with bolts have characterized the monolithic damping factor as 0.03% [62] to 0.0991% [63] for the first bending mode and 0.04% [62] to 0.0505% [63] for the second bending mode. Further complicating the issue, the low amplitude damping factor can be extremely sensitive to the test setup [64]. Given the significant range and dependence on the test setup, here, the lowest experimental values of the jointed structure (e.g., see Figure 7c) are adopted as the low amplitude damping or 0.087% for the first bending mode and 0.034% for the second bending mode. Therefore, the low amplitude damping cannot be considered a prediction of the present model.

3.2 Surface Processing

Surface scans are processed to determine asperity properties and the mesoscale topology for the friction model. An overview of the procedure is outlined in Figure 8. The interfaces of both half beams are scanned before testing in twelve patches with a KEYENCE VR-5100 White Light Interferometer. The scans are conducted with resolutions of 23.6 μm in the xy-plane and 4 μm in the vertical direction. The scanned patches are then stitched together into a single interface scan and outliers are eliminated [3, 38].[17] The patches do include some overlapping area that is not eliminated at this stage.

Using all of the scan points and conducting all subsequent steps in MATLAB, a least squares plane is fit to each side of the interface. This plane is then rotated to be parallel to the xy-plane, and the data from each patch is interpolated onto a regular grid[18] of the same resolution as the original scan data using natural interpolation of scattered points [65]. At this point, the outer 0.5 mm of data from the nominal interface size is trimmed off of each side and the holes are enlarged to a radius of 5 mm. This eliminates the noisy data around the edge of the scans as the flat interface transitions to the vertical sides of the beams and holes.

3.2.1 Mesoscale Topology

Previous studies have shown significant shifts in modal frequency for changes to the mesoscale topology [2, 3, 59, 66]. To characterize the mesoscale topology for the present experiments, the data from the regular grid within each patch is combined into a single matrix eliminating data points from the scan of each patch that overlap with other patches. At this stage, height data for the holes is filled in using natural interpolation of scattered points [65], and the scan data is extrapolated back to the nominal size of the interface using the nearest point in the grid data. A 2D-Gaussian image filter is applied to the interface with a standard deviation of $\sigma = 215$ points, a length of 5.074 mm, and a filter support of $6\sigma + 1$ points to smooth the

---

[17] The exact details of these processing steps in MATLAB can be found in [3].

[18] The rotations up until this point have perturbed points from a perfect grid.

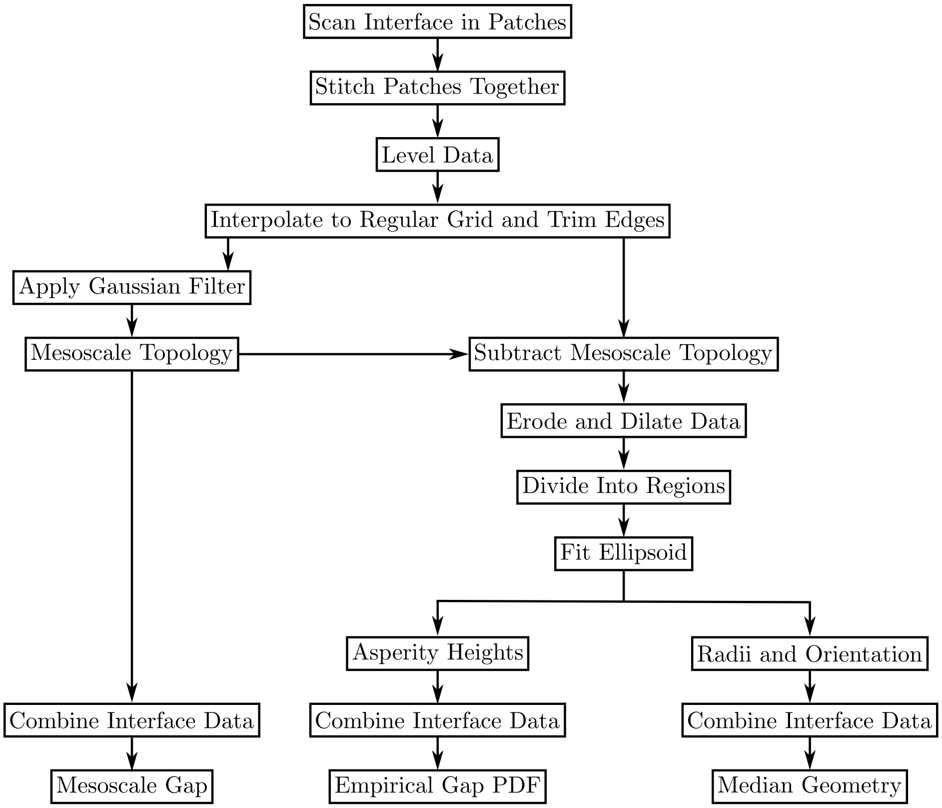

Figure 8: Overview of surface processing procedure.

interface representation.[19] Finally, the mesoscale topology is represented by using a linear, two-dimensional interpolation of the filtered height data. This produces a mesoscale topology that is independent of the interface mesh unlike previous studies that develop the mesoscale topology based on the interface mesh [2, 3]. Furthermore, the filtering process should limit any dependency of the mesoscale topology on the measurement length scale, potentially allowing for coarser measurements to be taken of the as-built topology compared to those required to characterize the statistical asperity properties.

3.2.2 Asperity Identification

To identify asperities,[20] the height at each xy-location on the regular grid is taken as the height after leveling minus the height of the mesoscale topology at that point. Then, the full interface is divided into regions of potential asperities by applying an identification algorithm based on the watershed algorithm [3, 68]. First, this process smooths the data by eroding and then dilating using a 2×2 square pattern. Next, the Sobel gradients are calculated at each point. Finally, the watershed algorithm is applied to divide the domain

---

[19] For reference, a continuous Gaussian filter attenuates wavelengths shorter than 2σ by greater than two orders of magnitude [67].

[20] Given the resolution of the measurement, only asperities larger than a certain threshold are able to be measured. However, the method used shows some improvements over other methods in limiting the dependency on the measurement scale [68].

based on the Sobel gradients.

Each potential asperity is then fit with an ellipsoid of the form

$$\frac{(x-b_x)^2}{a_{xx}} + \frac{(x-b_x)(y-b_y)}{a_{xy}} + \frac{(y-b_y)^2}{a_{yy}} + \frac{(z-b_z)^2}{a_{zz}} = 1 \tag{51}$$

using the total least squares fit [3]. Fits are rejected if they are based on fewer than 9 points, any of the ellipsoid axes are not positive finite values, the center of the ellipsoid is above the mean vertical heights of the fitted points (this implies a valley), there are a fewer than 3 unique x or y values,[21] or if the center is outside the range of the bounding rectangle of the fitted x and y coordinates.

To characterize the orientation of the ellipsoids, an angle α in the range $(-\pi/2, \pi/2]$ is measured counterclockwise from the positive x direction to the short principal semi-axis. For contact calculations, the large and small principal radii of curvature, R' and R'' respectively, at the peak are

$$R' = \frac{a_1^2}{a_{zz}} \tag{52a}$$

$$R'' = \frac{a_2^2}{a_{zz}}, \tag{52b}$$

where a_1 and a_2 are the large and small principal semi-axes of the ellipsoid in the xy-plane and a_{zz} is the semi-axis aligned with the z-direction. The height of the asperity is $h_z = b_z + a_{zz}$ corresponding the center of the ellipsoid fit plus the length of the vertical semi-axis. This height is the residual height of the asperity relative to the mesoscale topology.

3.2.3 Full Asperity Statistics

The two sides of the interface are considered to be two realizations of the same random process. Therefore, the data sets are combined and processed to produce one set of asperity properties for use on both sides of the interface. The principal radii are taken to be the median values of the principal radii of the combined list of all asperities. The area density of asperities is taken to be the total number of asperities divided by the total area searched for asperities.

Next, a probability distribution function (PDF) of the gap between two asperities when the interfaces are brought together without the mesoscale topology is generated. The residual heights of the asperities are shifted to have zero median and the lists are combined for the two sides of the interface. Then a full list of possible gaps is generated by taking the negative of each residual height minus all of the residual heights. Outliers of both small and large initial gaps are then eliminated from the list.[22]

This final list of gaps is then normalized to be between zero and one with the range of gaps being recorded as the maximum possible gap (the minimum gap is set to zero). The normalized set of gaps is fit

---

[21] Having only two rows or columns of points resulted in fits with a_{zz} on the order of meters due to the ill-conditioned nature of the problem.

[22] Taking the interquartile range (IQR) as the distance between the first and third quartiles, outliers are defined as values less than the first quartile minus 3×IQR or greater than the third quartile plus 3×IQR.

with an empirical PDF using an Epanechnikov kernel function and a support of [0, 1] [69]. As a practical note, computer memory constraints prevented calculating the empirical PDF using all of the normalized gap values. Instead, the full list was sorted and 10^5 approximately equally spaced points[23] were used to fit the PDF. The choice of the empirical PDF differs from previous studies considering a non-Gaussian distribution of asperity heights that used Pearson's system [27, 29] or Johnson's system [25, 32] to generate the PDF. Such approaches only match the mean, standard deviation, skewness and kurtosis of the desired distribution without necessarily matching the full shape. Conversely, the empirical PDF produces a precise representation of the measured distribution without these complications. A single gap PDF is generated for use everywhere on the interface so that the PDF represents the fabrication processes and thus is suited to industrial applications. This differs from other attempts to predict the response of the BRB using different asperity height distributions in each ZTE and thus are limited to predicting the response of structures with detailed surface scans [2, 3].

4 Solution Methods

The system behavior is analyzed through a combination of three different solution techniques. First, a nonlinear prestress analysis provides initial guesses for the other solution techniques (see Section 4.1). Furthermore, a linearized eigenvalue analysis around the prestressed state provides consistent low-amplitude frequencies with minimal computational cost. Second, a Quasi-Static Modal Analysis (QSMA) technique allows for the calculation of amplitude dependent modal frequency and damping characteristics with lower computational cost compared to frequency or time domain methods for the models using elastic normal contact (see Section 4.2) [70]. Finally, the extended periodic motion concept (EPMC) is used to characterize the models that include normal plasticity in the frequency domain (see Section 4.3) [71]. While EPMC is more computationally expensive than QSMA methods, the QSMA methods failed to converge for the models including plasticity since the prestressed displacements are coupled to the maximum normal displacements. Further discussion on the comparisons between the QSMA and EPMC methods can be found in [70]. Both the QSMA and EPMC methods solve for the system dynamics simultaneously considering both the prestress forces due to applied bolt torques and the dynamic forces. This differs from other studies that only consider the nonlinear dynamics as a perturbation around the prestressed state [4, 72].

4.1 Prestress Solution

For each of the solution steps, the reduced order model of the system (described in Section 3) with N DOFs is represented by the $N \times N$ mass $\boldsymbol{M}$ and stiffness $\boldsymbol{K}$ matrices. The prestress solution solves for static

---

[23] Since the number of potential asperity interactions could not be evenly divided into the $(10^5 - 1)$ segments, 10^5 values are calculated from dividing the maximum number of points into segments and rounding each value to obtain an index of which point to include in the fitting.

displacements $\underset{\sim}{u}_s$ that satisfy

$$\boldsymbol{K}\underset{\sim}{u}_s + \underset{\sim}{f}_{nl} - \underset{\sim}{f}_s = 0, \tag{53}$$

where $\underset{\sim}{f}_{nl}$ are the nonlinear friction forces described in Section 2 and $\underset{\sim}{f}_s$ are the static prestress forces. A vector of unit prestress forces applied to the bolt is generated as part of the model reduction step. This is then scaled by the average measured bolt preload force of 12.249 kN for application in the model. Here, the tangential tractions are set to zero for the prestress analysis based on previous work that suggested that RQNMA converges better using a conservative prestress analysis [7].

4.2 Quasi-Static Nonlinear Modal Analysis (QSMA)

QSMA methods were inspired by the implicit condensation method [73] and then developed into current methods [4, 74, 75]. The present study uses a QSMA method based on Rayleigh Quotients (RQNMA) that has been shown to provide more accurate properties than other QSMA methods [70]. At a prescribed modal amplitude q, RQNMA solves [70]

$$\boldsymbol{K}\underset{\sim}{u} + \underset{\sim}{f}_{nl} - \lambda\boldsymbol{M}\left(\underset{\sim}{u} - \underset{\sim}{u}_s\right) - \underset{\sim}{f}_s = 0 \tag{54a}$$

$$\left(\underset{\sim}{u} - \underset{\sim}{u}_s\right)^T \boldsymbol{M}\left(\underset{\sim}{u} - \underset{\sim}{u}_s\right) - q^2 = 0 \tag{54b}$$

for unknown displacements $\underset{\sim}{u}$ and Lagrange multiplier λ where $\underset{\sim}{u}_s$ is calculated with (53). To characterize the behavior at a desired amplitude q_0, the prescribed amplitude q is cycled between $\pm q_0$ until the value of λ has converged. The modal frequency is then calculated as

$$\omega_n(q_0) = \frac{\sqrt{\lambda(+q_0)} + \sqrt{\lambda(-q_0)}}{2} \tag{55}$$

based on the final final evaluations at $\pm q_0$. The nonlinear mode shape, $\phi(q_0)$, is taken to be

$$\underset{\sim}{\phi}(q_0) = \frac{\underset{\sim}{u}(+q_0) - \underset{\sim}{u}(-q_0)}{2q_0}. \tag{56}$$

for displacement vectors $\underset{\sim}{u}$ at both extremes of the cycle ($\pm q_0$). For plotting, a $1 \times N$ recovery vector $\underset{\sim}{R}$ is used to determine the displacement at the accelerometer since the DOF at the accelerometer is not preserved in the ROM.[24] By analogy to a linear system, this is converted to an acceleration, a, as

$$a(q_0) = q_0 \left[\omega_n(q_0)\right]^2 \left[\underset{\sim}{R}\underset{\sim}{\phi}(q_0)\right] \tag{57}$$

to use as the amplitude for plotting comparisons with the experimental data.

The modal dissipation $D(q_0)$ is calculated by integrating the quantity λq over the final cycle. The dissipation is converted to a damping factor $\zeta(q_0)$ by analogy to linear systems as

$$\zeta(q_0) = \frac{D(q_0)}{2\pi(\omega_n(q_0)q_0)^2} + \zeta_{0,exp}, \tag{58}$$

---

[24] Including the accelerometer node in the ROM would require fixing it to have zero displacement when calculating the fixed interface modes (see Section 3.1) and thus lead to less physical fixed interface modes. Thus the accelerometer node is not included in the ROM [2, 3, 7, 56].

where $\zeta_{0,exp}$ represents an assumed level of modal damping at zero amplitude that is not caused by the bolted joint (see Section 3.1.2). Further discussion and examples of the application of RQNMA can be found in [7, 70].

4.3 Extended Periodic Motion Concept (EPMC)

EPMC extends previous frequency domain methods to the case of lightly damped systems [71], and is considered to be more accurate than the quasi-static methods [70]. EPMC has unknowns corresponding to each of the DOFs for the zeroth harmonic, $\underset{\sim}{u}_0$, and the sine and cosine components of each higher harmonic (i.e., $\underset{\sim}{u}_{nc}$ and $\underset{\sim}{u}_{ns}$ for the nth harmonic respectively). For a maximum harmonic of H and N DOFs, there are a total of $(2H+1)N+2$ unknowns corresponding to the unknown displacement coefficients, the natural frequency ω_n, and required mass proportional forcing ξ. This results in significantly larger systems and more computation than RQNMA, which only has $N+1$ unknowns at each step.

For EPMC, a proportional damping matrix $\boldsymbol{C}$ is generated such that the linear analysis around the prestressed state matches the low amplitude damping factors of the first two elastic bending modes. The proportional damping matrix is

$$\boldsymbol{C} = \alpha_d \boldsymbol{M} + \beta_d \boldsymbol{K_{pre}} \tag{59}$$

where the proportionality coefficients are calculated based on the Jacobian stiffness $\boldsymbol{K_{pre}}$ after prestress.[25] Given the first two bending natural frequencies of ω_1 and ω_2 and damping factors for the first two modes of $\zeta_{0,1}$ and $\zeta_{0,2}$, the coefficients are calculated as

$$\begin{bmatrix} \frac{1}{2\omega_1} & \frac{\omega_1}{2} \\ \frac{1}{2\omega_2} & \frac{\omega_2}{2} \end{bmatrix} \begin{bmatrix} \alpha_d \\ \beta_d \end{bmatrix} = \begin{bmatrix} \zeta_{0,1} \\ \zeta_{0,2} \end{bmatrix}. \tag{60}$$

EPMC solves the set of equations [71]

$$\begin{gathered} \boldsymbol{K}\underset{\sim}{u}_0 + \underset{\sim}{f}_{0,nl} - \underset{\sim}{f}_s = 0 \\ (-n^2\omega_n^2\boldsymbol{M} + \boldsymbol{K})\underset{\sim}{u}_{nc} + n\omega_n(\boldsymbol{C} - \xi\boldsymbol{M})\underset{\sim}{u}_{ns} + \underset{\sim}{f}_{nc,nl} = 0 \quad \forall n \in \{1,\ldots,H\} \\ (-n^2\omega_n^2\boldsymbol{M} + \boldsymbol{K})\underset{\sim}{u}_{ns} - n\omega_n(\boldsymbol{C} - \xi\boldsymbol{M})\underset{\sim}{u}_{nc} + \underset{\sim}{f}_{ns,nl} = 0 \quad \forall n \in \{1,\ldots,H\}. \end{gathered} \tag{61}$$

Here, the nonlinear forcing terms for each harmonic (e.g., $\underset{\sim}{f}_{1c,nl}$) are obtained via the Alternating Frequency-Time (AFT) procedure described below [76–78]. To define a unique solution, constraints are imposed to obtain an amplitude q_0 and a fixed phase requiring

$$\underset{\sim}{u}_{1c}{}^T\boldsymbol{M}\underset{\sim}{u}_{1c} + \underset{\sim}{u}_{1s}{}^T\boldsymbol{M}\underset{\sim}{u}_{1s} - q_0^2 = 0 \tag{62a}$$

$$\underset{\sim}{f}_{dyn}{}^T\underset{\sim}{u}_{1c} = 0, \tag{62b}$$

---

[25] The normal stiffness is calculated on the elastic unloading curve for the plastic normal contact models.

where $\underset{\sim}{f}_{dyn}$ defines a forcing direction to provide a phase constraint on the first harmonic. EPMC does not include any applied forcing; $\underset{\sim}{f}_{dyn}$ serves as an arbitrary constraint to eliminate solutions with the same amplitude, but different phases. The present work uses EPMC as implemented by [3].

For plotting, the acceleration at the accelerometer is calculated based only on the first harmonic of the response as

$$a = \omega_n^2 \sqrt{(\underset{\sim}{R}\underset{\sim}{u}_{1c})^2 + (\underset{\sim}{R}\underset{\sim}{u}_{1s})^2}, \tag{63}$$

and all of the variables are evaluated at an amplitude q_0 of interest. This approach is consistent with the processing of the experimental data, which is first filtered around the mode of interest and thus eliminated any amplitude contributions of the higher harmonics of the mode of interest.[26]

4.3.1 Alternating Frequency-Time (AFT) Procedure

The AFT procedure is used to calculate the Fourier coefficients of the nonlinear forces in (61) [76–78]. The displacement time series at each quadrature point of the reduced mesh is evaluated at N_t times spaced at intervals $\Delta t = T/N_t$ through a single cycle of time T. The friction model is applied to the displacement time history to calculate frictional tractions in each element of the ROM. The Fourier coefficients of the tractions are calculated and then integrated into nodal harmonic forces acting on the DOFs.

The frictional tractions are evaluated for up to ten consecutive cycles or until the tractions at the beginning and end of the cycle are converged. Generally, the slider representation used with the present model converges within two cycles [78]. Here, the Fourier coefficients are evaluated only for the final converged cycle of frictional tractions.

Before evaluating the frictional forces, the previous tangential displacements are initialized to the zeroth harmonic values and the normal displacement equal to the maximum normal displacement for the entire time series. The tangential forces of each asperity are initialized to zero and the normal force is initialized to the appropriate value based on the normal loading model. The tangential initialization ensures that the frictional evaluation is not dependent on the phase[27] or the initial coordinate system[28] since both are arbitrary constructs of the mathematical problem. The normal initialization ensures that plasticity models are always calculated on the same elastic normal unloading curve and thus eases the calculation of the derivatives with respect to the harmonic coefficients.

---

[26] The numerical procedure still differs from the experimental tests in that only one mode is excited at a time.

[27] As would happen if the first friction evaluation was at the first set of tangential displacements.

[28] As would happen if the first friction evaluation used zero displacement as the history inputs.

5 Results

5.1 Surface Processing Results

Prior to calculating the system response, the surface scans are processed with the procedure described in Section 3.2 to obtain the necessary parameters using an erosion size of a 2×2 grid. First, Figure 9a shows that the calculated mesoscale topology results in a gap of approximately 100 μm between the two surfaces around the central bolt. While most variation in the mesoscale topology occurs along the x-direction, deviations on the order of 5e-6 m in the y-direction break symmetry. Figure 9b illustrates an example ellipsoid fit to the scan data. The surface processing procedure calculates a smooth PDF for the initial gap between asperities as shown in Figure 9c. Finally, from Figure 9d, the asperity rotation angles[29] are mostly around $\pi/2$, so this is adopted for the majority of simulations. Table 2 summarizes the other relevant asperity statistics and shows that the asperities differ significantly from spheres with the larger principal radii being 5.38 times larger than the smaller principal radii. Unlike previous studies that have employed different asperity statistics in each ZTE [2, 3], the values presented in Table 2 are the statistics derived for the full interface as described in Section 3.2 and are applied identically to all ZTEs.

Table 2: Summary of asperity statistics for the baseline erosion size of 2 points.

Parameter	Description	Value
R'	Large principal relative radius of curvature	3.167 mm
R''	Small principal relative radius of curvature	0.588 mm
R_e	Equivalent radius	1.365 mm
z_{max}	Maximum asperity gap	28.05 μm
α	Angle between x+ and short principal axis	$\pi/2$ rad
η	Area density of asperities	1.371e6 m^{-2}

5.2 Elastic Modeling Results

The nonlinear trends in modal frequency and damping are characterized for the fully elastic asperity models described in Section 2 using RQNMA (see Section 4.2). For RQNMA, the dissipation is calculated using 10 Legendre-Gauss-Lobatto quadrature points per loading or unloading branch of the hysteresis loop. The calculation of the hysteresis loop is repeated up to four times to converge the calculated damping factor. If

---

[29] Note that $\alpha = \pi/2$ is equivalent to $\alpha = -\pi/2$ since the ellipsoids are symmetric about both their local x_1 and y_1 axes.

[30] Note that there are variations on the order of 5e-6 m in the y-direction that are not visible compared to the large variations in the x-direction.

[31] The right axis corresponds to the empirical PDF evaluated for the normalized gap value (i.e., for gap z_i the right axis is $p(z_i/z_{max})$)

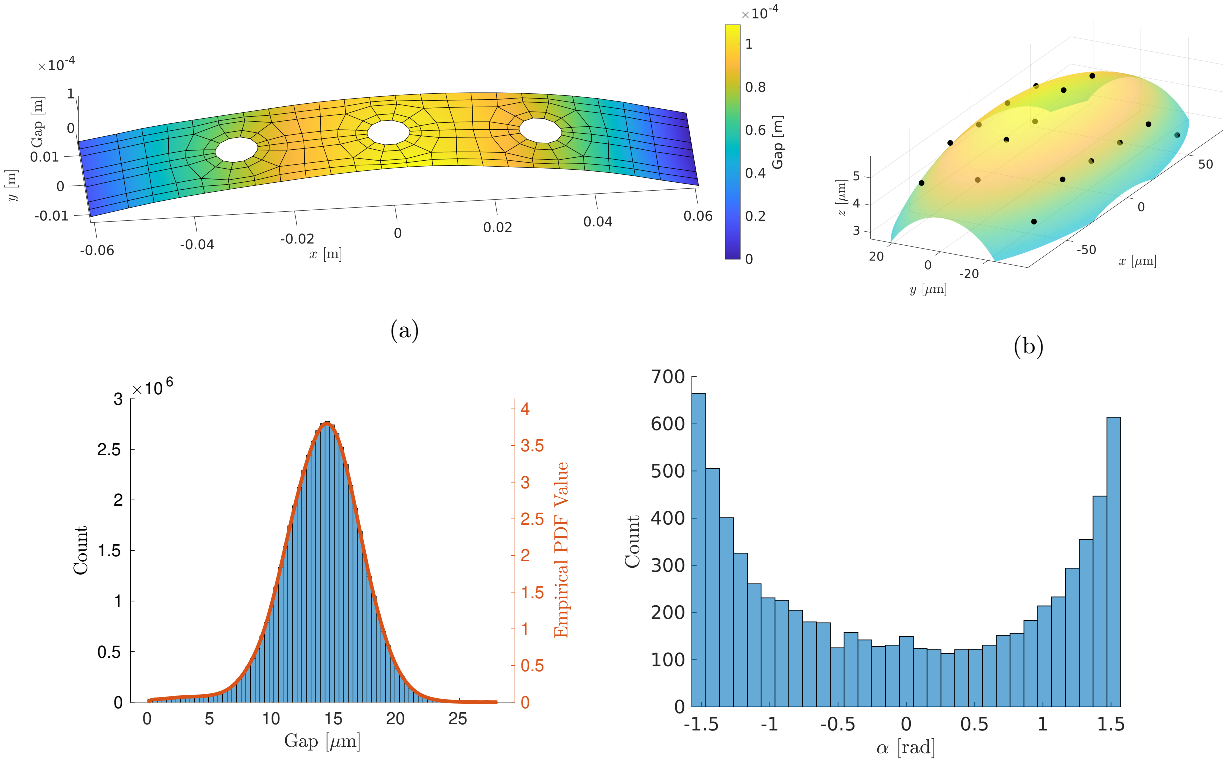

(a)

(b)

(c)

(d)

Figure 9: Results of surface processing (a) mesoscale gap between the two interfaces on the 232 ZTE mesh,[30] (b) example asperity fit, (c) asperity gap probability distribution,[31] (d) asperity orientation angle.

the fractional change in damping factor is less than 1e-5, then the calculation is exited before the final loop iterations are completed.

Since most predictive friction coefficients are based on plasticity [12, 24], a satisfactory prediction of the friction coefficient cannot be made for the purely elastic case. As an alternative, Figure 10 shows the backbones for several different friction coefficients using the tangent asperity model. As expected, decreasing the friction coefficient results in a larger decrease in frequency and a larger increase in damping as the system starts to slip sooner. Here, a friction coefficient of $\mu = 0.03$ most closely matches the frequency shift and nonlinear damping of the experimental data, therefore this friction coefficient is used for subsequent backbones. While this coefficient is small, fretting experiments do not necessarily represent the same frictional processes [16, 17, 41, 79] and some experiments have shown very small friction coefficients in the presence of plasticity [80]. Additionally, since hammer impacts are used to characterize the behavior, only a few thousand cycles of the first mode of vibration are observed, with many in a near stuck condition, and thus the friction coefficient may not have increased to a steady-state value as is common with fretting experiments. Furthermore, small friction coefficients have been used to match experiments for other experimental data sets with the BRB [2]. Alternatively, it is possible that the friction coefficient is being used to capture additional physical phenomena beyond proportional slipping, and thus future work should further investigate the frictional slip mechanisms.

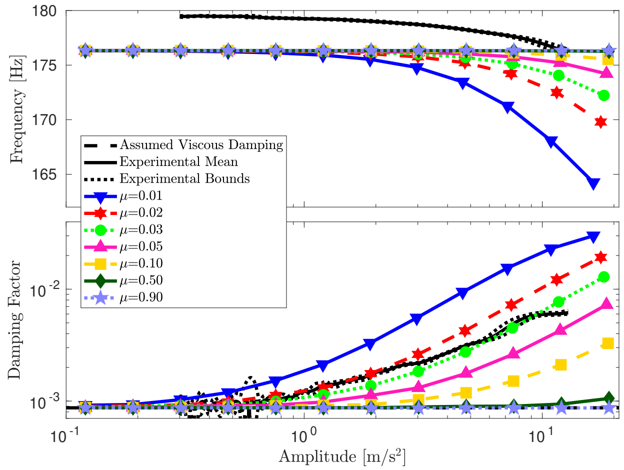

Figure 10: Backbones for different friction coefficients using the decoupled tangent model.

The low amplitude frequency of 176.3 Hz is 3.2 Hz lower than the experimental frequency, but similar to that of previous predictions for the BRB [2, 3]. The error here can be attributed to simplifications in the model such as the lack of plasticity. While [3] produces nearly the exact low amplitude frequency, the tangential stiffness was chosen to be the highest from three different models and thus results in a slightly stiffer system. The present model has the potential to predict the response of new systems that activate the same frictional mechanisms since the models are physically derived. One caveat is that the physics included in the present model is deduced based on looking at one category of lap joints, so it is not clear how applicable the models are to other joints (e.g., flange joints). While the friction coefficient is not predicted, the qualitative behavior of the frequency backbone matches the experimental behavior of a smooth and gradual decrease in modal frequency. This can be attributed to the microslip nature of the model compared to previous macroslip models that struggled to capture the transition [2, 3].

The present friction model does not dissipate significant energy at low amplitudes, so the low amplitude damping factor is dominated by that of the monolithic structure. Therefore, the close match to the experimental damping at the lowest amplitudes is not a prediction of the model, but rather due to the choice of viscous damping factor to match the experimental data (see Section 3.1.2). The shift in damping factor is caused by the friction model and reflects the smooth qualitative behavior of the experimental trends. This is a clear improvement over the sudden increases in damping seen in macroslip models [2, 3, 7]. Furthermore, it is promising that the same friction coefficient of 0.03 matches both the frequency shift and the damping factor, whereas model fitting must often make a trade-off between the two [7]. The experimental damping factor appears to level off at the highest amplitude levels unlike the numerical models. However, this behavior of the backbone is sensitive to the processing parameters and thus is not well characterized by the present set of experiments.

Using a friction coefficient of 0.03, four different asperity models are compared in Figure 11a. Here, the Mindlin-Iwan models each use 100 sliders per asperity. At the lowest amplitude level, all four models produce frequencies within 0.2 Hz with the slight differences being attributed to the outermost contact rings of some asperities slipping. As the amplitude increases, the tangent model produces higher frequencies than the other models with a maximum difference between models of 0.6 Hz. As expected from Section 2.2.4, the MIC model produces frequencies between the tangent and MIF models since it over-predicts the secant stiffness of the partial slip displacement until the start of macroslip. At intermediate amplitude levels, the MIF models produce up to 28% larger damping factors than the tangent model. However, at the highest and lowest amplitude levels, the differences in damping factor are insignificant. Here, the benefit of the MIF models can be attributed to incorporating an appropriate microslip model for each asperity compared to only obtaining the microslip behavior from having a distribution of asperity heights in the tangent model. Lastly, tangential coupling of the friction model using (45) instead of (37) has a minimal effect on the MIF model since the majority of the tangential displacement is expected to be aligned with the x-axis and thus with the local coordinate system of the asperities.

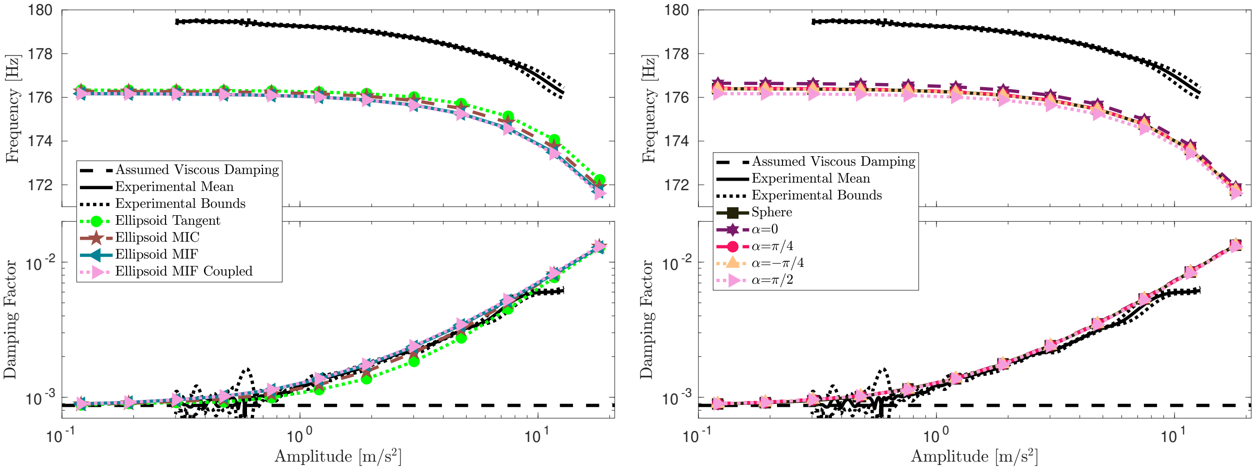

(a) (b)

Figure 11: Backbones for (a) different tangential asperity models and (b) different rotation angles α using the tangentially coupled MIF model. The coupled MIF model use (45) locally instead of (37) for the uncoupled MIC and MIF models.

Figure 11b compares the effect of different asperity orientation angles, all using the coupled MIF model. A tangentially coupled model is required for testing different rotation angles since the uncoupled model effectively increases the slip limit by 41% at an angle of $\pi/4$ from the principal axes that the friction model is evaluated along. The cases of spherical asperities and ellipsoids at angles of $\alpha = \pm\pi/4$ all yield nearly[32] identical frequency backbones. The case of $\alpha = 0$ yields the highest set of frequencies ranging from 0.25 Hz

---

[32] The cases of $\alpha = \pm\pi/4$ are different only in that the mesoscale topology is not symmetric.

to 0.16 Hz higher than the case of spheres. Alternatively, the case of $\alpha = \pi/2$ yields the lowest frequencies ranging from 0.23 Hz to 0.14 Hz lower than the case of spheres. The largest differences in frequency are seen at the lowest amplitudes with the models approaching similar values at higher amplitude levels. The effect of rotation angle is expected since ellipsoidal asperities are stiffer along the axis aligned with the small principal radii of curvature (the x-axis for $\alpha = 0$) than the axis aligned with the large principal radii of curvature (the x-axis for $\alpha = \pi/2$). The amplitude dependent damping for all of these cases is indistinguishable. Thus, for the elastic contact models, asperity orientation has a negligible influence on the dynamics of the system. This gives some confidence in being able to predict the dynamics of a system that has not yet been fabricated.

5.3 Plastic Modeling

Following the elastic investigations, plastic behavior is incorporated into the asperity contact model (see Section 2.1). Here, EPMC (see Section 4.3) is used to determine the nonlinear modal characteristics. The results between EPMC and RQNMA are verified in Figure 12 for the elastic case and show good agreement.

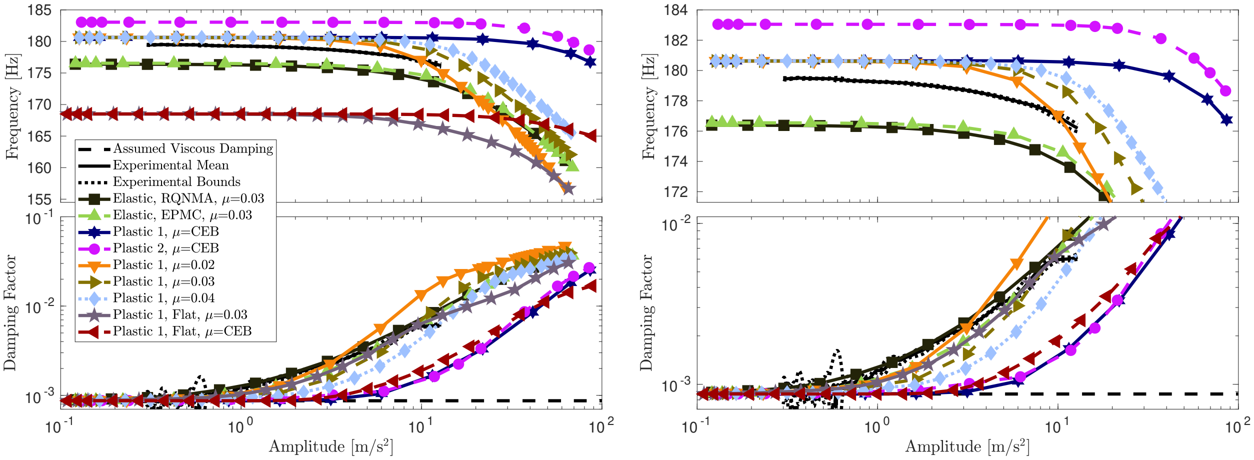

(a) (b)

Figure 12: Backbones illustrating the impact of different asperity physics: (a) full backbones and (b) zoomed in on plots.

Two sets of plasticity material properties are used for the yield strength S_{ys} and hardening modulus E_t. The material properties for the case of "Plastic 1" are $S_{ys} = 330$ MPa and $E_t = 620$ MPa [57], and for "Plastic 2," the material properties are $S_{ys} = 150$ MPa and $E_t = 3500$ MPa [58]. Here, incorporating plasticity results in a notable increase in the low amplitude frequency with a more significant effect for the lower yield strength of the "Plastic 2" parameter set. This behavior can be attributed to the plastic deformation allowing for further contact between asperities while the strain hardening minimizes the loss of normal stiffness on the unloading curve. These two cases also highlight that uncertainty about the plastic parameters of the asperities can result in significant changes in the response frequency and thus further work is necessary to accurately capture the plastic behavior of the asperities. Due to work hardening and grain refinement from the manufacturing and polishing processes, it is possible for the material properties (specifically the properties that govern the plastic response - yield strength and hardness) at the surface of the interface to vary significantly compared to the bulk of the material [41].

As with the elastic results, the plastic results can be run for a number of constant friction coefficients to obtain frequency and damping shifts comparable to the experimental data. As a more predictive option, the CEB friction model is considered. However, this results in frequency and damping shifts at a significantly higher amplitude than the experimental data indicating that it is over-predicting the friction coefficient. Therefore, further investigation is required to understand what mechanisms govern the slip limit of contacting asperities. The choice of the CEB model should not be considered a completely blind prediction since it was chosen from the four models presented in [24] as the only one with the potential of achieving friction coefficients as low as those fit for the elastic results.

Figure 12 also presents results for the plasticity model and a flat interface (e.g., zero nominal gap replacing that of Figure 9a). The flat interface results in significantly lower frequencies than the measured mesoscale topology. This is consistent with experimental results that have shown increases in frequency when the interface initially comes into contact on the edges [59]. It is promising that the model agrees with the qualitative behavior of other experiments and the present work further highlights the importance of capturing the as-built mesoscale topology rather than assuming the nominally flat geometry.

5.3.1 Hysteresis Loops

The present section investigates the form of the hysteresis loops and the spatial distribution of the dissipation. For each of the considered models, a single amplitude level is chosen to have a frequency shift of approximately 3.5 Hz. However, given the continuation algorithm used with EPMC, solutions are not known at exactly the same frequency shifts, damping levels, or amplitudes. Thus the total dissipation cannot be directly compared between models throughout this section. However, the spatial distribution of the dissipation is of primary interest and can be compared between models since they are within a similar loading regime.

For the plasticity model with a constant friction coefficient, the hysteresis loops all have relatively normal and symmetric behavior (see Figure 13). The elastic model with a constant friction coefficient showed very similar behavior and is omitted for brevity. The dissipation primarily comes from the left and right most columns of elements. This is expected since the mesoscale topology (see Figure 9a) results in the full interface remaining in contact and the edges of the interface generally have the largest tangential displacements. For the plasticity model with the flat interface (i.e., no mesoscale topology) in Figure 14, the dissipation is more regularly distributed. For the flat interface, the pressure on the left and right most columns of elements is relatively low and thus limits the amount of energy dissipated. Furthermore, this pressure varies throughout the cycle resulting in some clearly asymmetric and non-Masing hysteresis loops such as Figure 14c. Moving towards the center of the interface, the next two columns of elements on both sides dissipate a significant amount of energy since they still enter slip, but do not lose normal pressure and thus can dissipate more energy. Finally, the central region of the interface remains nearly stuck and thus dissipates little energy.

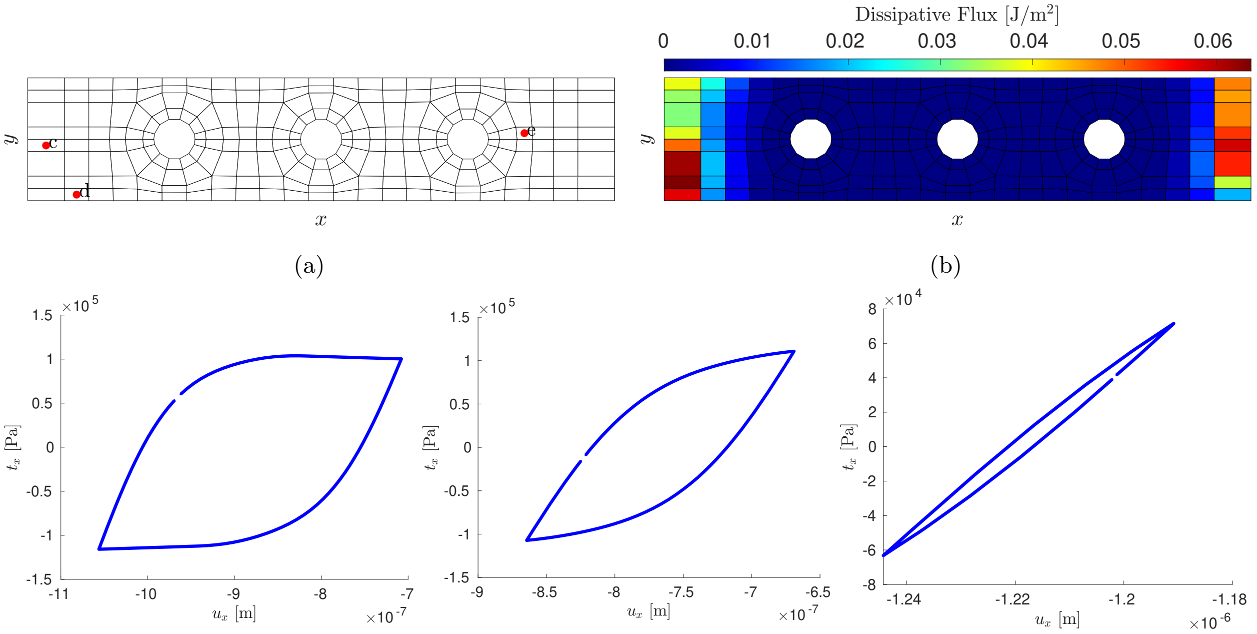

(a) (b)

(c) (d) (e)

Figure 13: Example hysteresis loops for the plastic 1, $\mu = 0.03$ case (a) mesh locations for corresponding to subplots (c)-(e), (b) spatial distribution of energy dissipation, and (c)-(e) example hysteresis loops for locations marked in (a).

Using the CEB friction model results in a wide variety of hysteresis loops (see Figure 15). Many of the hysteresis loops decrease to zero traction between reversals due to the maximum normal displacement being reached (and thus the friction coefficient becoming zero). These hysteresis loops all show clearly non-Masing behavior and thus motivate the use of the proposed general framework rather than the Masing assumptions. Figure 15g shows an interesting response due to significant contributions of higher harmonics, specifically, the second harmonic of the normal displacement. The hysteresis loops in Figure 15 are not mirrored along the x-axis (e.g., Figure 15(c) and Figure 15(f) are different) because the mesoscale topology is not symmetric about either axis (see Section 5.1). Since the CEB model in Figure 15 uses the mesoscale topology, the distribution of the dissipative flux is similar to that of Figure 13.

In general, the solutions with the CEB friction model included significantly more contributions of the higher harmonics than the constant friction coefficient models. This is likely a result of requiring significant changes in the normal displacement to avoid zero friction coefficients. The result is that the CEB friction model changes the behavior of the system significantly.

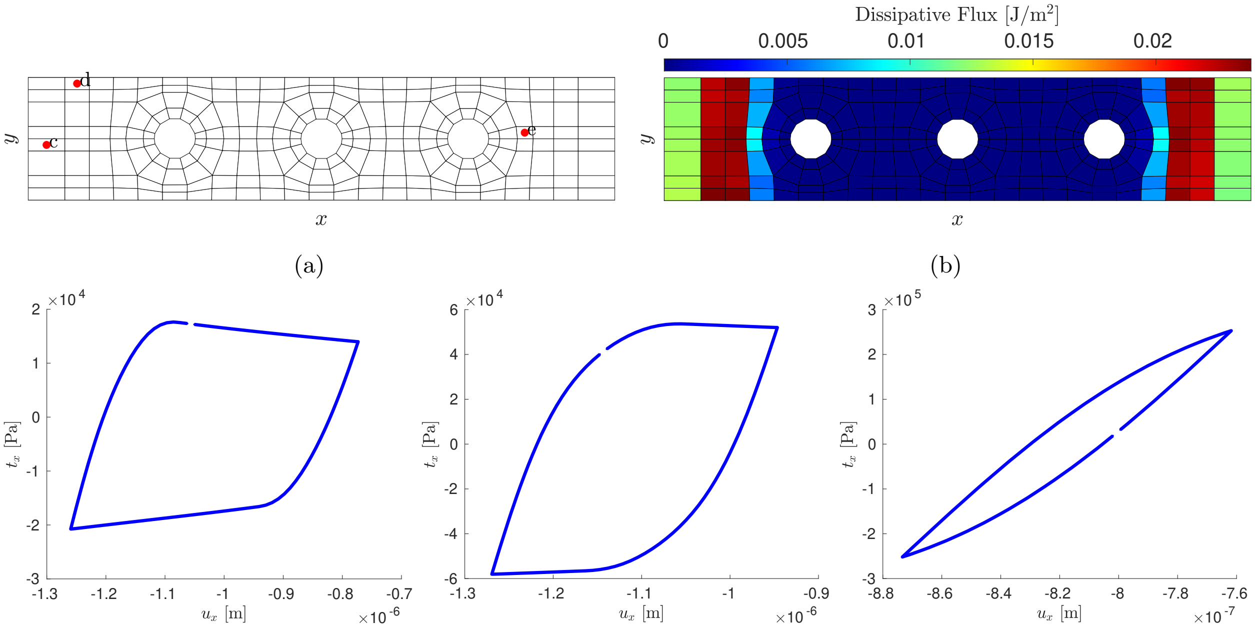

(a)

(b)

(c)

(d)

(e)

Figure 14: Example hysteresis loops for the plastic 1, $\mu = 0.03$, flat case (a) mesh locations for corresponding to subplots (c)-(e), (b) spatial distribution of energy dissipation, and (c)-(e) example hysteresis loops for locations marked in (a).

5.4 Asperity Length Scale

Tribological measurements are very sensitive to the length scale of measurement, and thus the identified sizes and density of asperities could vary significantly with different measurement techniques. To investigate the effect of asperity length scale, the erosion parameter in the surface processing algorithm is varied. Eroding a larger number of points eliminates small features and thus increases the size of the identified asperities while modifying the other surface parameters in a consistent way (e.g., decreasing asperity density). Figure 16 shows the backbones for four different erosion sizes with asperity parameters described in Table 3. Here, only the CEB friction coefficient is considered since it is unclear how the slip limit evolves as the asperity length scale varies. Furthermore, a constant friction coefficient can be fit to the experimental data, so its inclusion here would not be as informative.

Increasing the erosion size, corresponding to fewer larger asperities, decreases the frequency significantly. In addition, the CEB model predicts less slip at a given amplitude level as the asperity length scale increases. Here, the erosion size could be used as a free variable to match exactly the low amplitude frequency. However, the present work seeks to develop a physics-based model that is useful for future predictions and thus is not interested in fitting the experimental data. To improve the present model, future work should consider the length scale to capture the asperities. This may be related to improving the understanding of the plasticity and failure of smaller asperities, which could also improve predictions of plasticity based friction

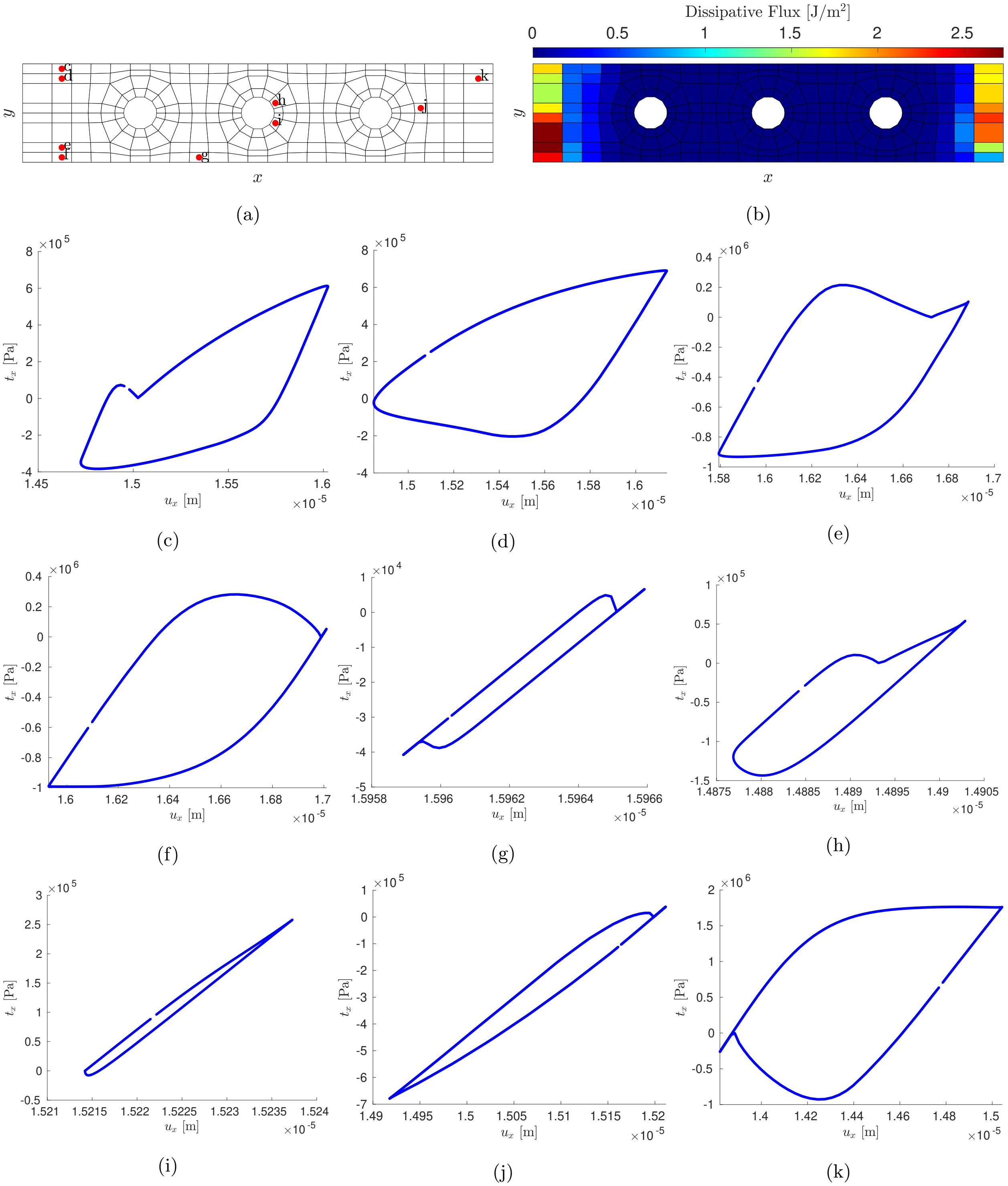

Figure 15: Example hysteresis loops for the plastic 1, μ = CEB case (a) mesh locations for corresponding to subplots (c)-(k), (b) spatial distribution of energy dissipation, and (c)-(k) example hysteresis loops for locations marked in (a).

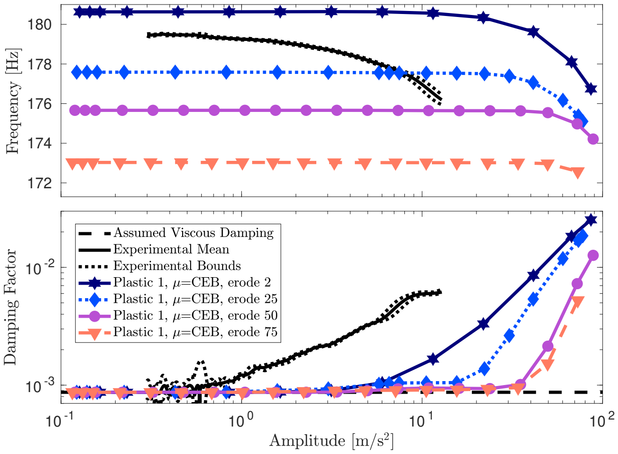

Figure 16: Backbones for different erosion sizes in the asperity identification algorithm. See Table 3 for the surface properties.

Table 3: Summary of asperity statistics.

Parameter	Description	Values			
	Erosion size (points)	2	25	50	75
R_e	Equivalent radius (mm)	1.365	9.819	23.80	29.93
z_{max}	Maximum asperity gap (μm)	28.05	25.85	24.36	27.61
η	Area density of asperities (m^{-2})	1.371e6	1.583e5	6.050e4	3.638e4

coefficients. Furthermore, preliminary analysis of scans before and after eight hours of shaker testing suggests that asperity sizes could increase beyond the range considered here [38]. This highlights the importance of capturing the length scale of asperities for accurately predicting the response for industrial applications.

5.5 Second Bending Mode

Five representative models are compared using EPMC (see Section 4.3) to experimental data for the second bending mode of the BRB in Figure 17. These models all show similar trends as when they are applied to the first bending mode. The "Plastic 1" case with the mesoscale topology closely matches the experimental data with a friction coefficient of 0.03. The fact that the same model matches both the first and second bending modes implies that some physical properties of the system are well captured. For the second bending mode, using either an elastic asperity contact model or a flat mesoscale topology results in frequencies notably lower than the experimental data. The CEB friction coefficient predicts a much higher slip limit than the other models and the experimental data. This is manifested in the predicted behavior of both the first and second bending modes using the CEB friction model. Finally, increasing to an erosion size of 75 shows a decrease in frequency and an increased slip limit for the CEB friction model compared to an erosion size of

2.

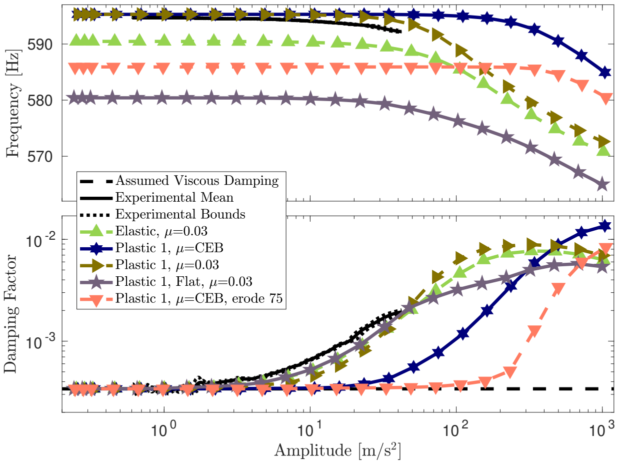

Figure 17: Backbones for the second bending mode run with EPMC.

5.6 Computation Time

The present section provides estimates of the computation time in Table 4. Surface processing (see Section 3.2) and RQNMA (see Section 4.2) computations are timed on the same desktop computer (Intel i7-10710U CPU, 1.10 GHz processor with 6 cores and 32 GB of RAM). The EPMC solutions (see Section 4.3) are too computationally intensive, and are thus run on a heterogeneous cluster with batch scheduling. Precise control of the assigned node is not possible resulting in only estimated times for EPMC. On the cluster, simulations use 64 GB to 800 GB of RAM and 16-40 cores at 2.1 to 2.6 GHz. During initial testing, some EPMC simulations ran out of memory when running on nodes with 32 GB of RAM, however 64 GB of RAM was sufficient.

The present model is significantly more computationally intensive than typical empirical models (e.g., elastic dry friction took 81 seconds to simulate in [7] on the same hardware). The EPMC models with the CEB friction coefficient generally had lower computation times than the other EPMC models, likely because there is less slipping and thus the system remains closer to the linear case. The EPMC times for Mode 1 show a significant spread since the parameters for the continuation algorithm are not fully optimized.

The present paper seeks to compare the fidelity of different modeling approaches, so the code is not optimized for performance. However, parallelism is exploited for some parts of the surface processing. For all friction evaluations, parallel for loops are used within MATLAB to spread the 232 friction evaluations (one per ZTE) across the available processors. MATLAB also automatically uses available cores for operations including to solve the systems of linear equations for each iteration update during the nonlinear solution. The Mindlin-Iwan models use vectorization for all of the sliders of a given asperity. All of the models use the same function for integrating over the asperity probability distribution, which cannot easily be vectorized given the Mindlin-Iwan models' use of vectorization. Vectorizing this calculation would likely result in notable

Table 4: Wall time for different portions of the computation. Mode 1 and mode 2 computation times with EPMC are similar and are reported in aggregate here. Both Mindlin-Iwan models require a comparable number of operations for each friction evaluation.

Computation Segment	Computer	Cores	Time
Surface Processing	Desktop	6	9.4 min
RQNMA Tangent Model	Desktop	6	26 min
RQNMA Mindlin-Iwan Fit Model	Desktop	6	3 hours
EPMC Models	Cluster	24	approx. 40 min-4 hours

speedups for friction evaluations using only the tangent asperity model.

5.7 Perspective and Outlook

The considered models require significantly greater computational effort than empirically calibrated models. However, industry, due to a variety of pressures, is moving away from conducting sufficient experiments for calibrated models [81]. Exacerbating the issue, calibrated models require significant amounts of data to be accurate for the range of operating conditions of a real structure. The goal of the present work is not to replace empirical modeling approaches, but to work towards a predictive model that can be applied without experimental dynamic data (e.g., before a structure is manufactured). To this end, only statistical properties of asperities are used across the whole interface as opposed to using different properties in each element as was done in [2, 3]. In future work, these properties could be identified based on manufacturing processes rather than scans of the final joint. However, statistics alone are not sufficient since the mesoscale topology of the as-built structure is needed to accurately capture the dynamic behavior. This emphasizes the notion expressed by the international joints community that joint interfaces need to be redesigned so that they are insensitive to mesoscale variations and are thus more predictable [82]. While the present work does not achieve a fully predictive model of the dynamics (e.g., the friction coefficient is still fit to experimental data), this work highlights improvements over previous techniques and future areas of research that could lead to fully predictive models.

To make predictions of the response of a structure with many joints, a future workflow may include simulating individual characteristic joints with a high fidelity physics-based model and then fitting simpler computationally efficient empirical models to those simulations. The ultimate goal is to supplement or even replace experimental data with high fidelity models in the surrogate system hypothesis [5] and then apply empirically fit models to joints within the larger assembly simulations. Such an approach would enable predictive modeling earlier in the design process before any prototypes are built and thus provide significant cost and time savings.

6 Conclusions

The major contribution of this paper is the development of a microslip rough contact model that can be applied to arbitrary loading conditions to model bolted structures. This model includes microslip due to both the distribution of asperity heights and a new slider representation of the Mindlin partial slip solution. This model is applied to a three bolt lap joint known as the Brake-Reuß Beam and presents a promising path towards a fully predictive model of the frictional interactions. The key conclusions are:

- The developed microslip rough contact model is capable of capturing the smooth trends in modal frequency and damping.
- Incorporating microslip at the asperity scale resulted in a notable increase in damping factor and frequency shift. However, given the current gap between the models and the experiments, it is reasonable to use the computationally faster stick-slip model for asperities.
- The ellipticity and orientation of the asperities has minimal effect on the frequency and damping factor.
- The rough contact modeling framework achieves a reasonable estimate of the low amplitude frequency. On the other hand, the low amplitude damping is not predicted by the model and is believed to be caused by other phenomena.
- Incorporating plasticity and the mesoscale topology both have a significant impact on the natural frequency. As neither the plastic properties of surface features nor the mesoscale features due to machining are known a priori, this represents the greatest impediment to having a fully predictive model.
- A statistical treatment of the asperities in the interface was sufficient for accurate predictions, implying that precise knowledge of the asperities is not needed for predictability.
- The CEB friction model significantly over-predicts the amplitude required for the frequency and damping shifts shown in the experimental data.
- The length scale of identification of asperities significantly affects the modal frequency and thus requires further characterization.

Future work could seek to reduce the errors in low amplitude frequency by incorporating additional physics such as oblique contact of asperities, asperity interactions or by characterizing asperity material properties distinct from those of the bulk material. Furthermore, new contact models are needed for the plastic loading and elastic unloading of ellipsoids and the tangential stiffness of asperities in both regimes. Additional investigation is also necessary to characterize the failure and relevant length scales of asperities to reduce uncertainty in input parameters and provide new potential slip limit models.

Through the development of a microslip rough contact model for bolted joints, this paper highlights a potential path for predictive modeling that is able to characterize both the low amplitude modal frequency and the qualitative behavior of the nonlinear modal frequency and damping factor, and thus represents a significant improvement in physics-based friction models for bolted connections. To aid in further development of rough contact models the code is publicly available [83].

Acknowledgments

The authors would like to thank Nidish Narayanaa Balaji, Iyabo Lawal, and Scott A. Smith for conducting experiments and sharing data for the Brake-Reuß Beam.

Funding: This material is based upon work supported by the U.S. Department of Energy, Office of Science, Office of Advanced Scientific Computing Research, Department of Energy Computational Science Graduate Fellowship under Award Number(s) DE-SC0021110. This work was supported in part by the Big-Data Private-Cloud Research Cyberinfrastructure MRI-award funded by NSF under grant CNS-1338099 and by Rice University. The authors are thankful for the support of the National Science Foundation under Grant Number 1847130.

References

[1] M. R. W. Brake, ed. *The Mechanics of Jointed Structures.* Springer, 2017.

[2] N. N. Balaji, W. Chen, and M. R. W. Brake. "Traction-based multi-scale nonlinear dynamic modeling of bolted joints: formulation, application, and trends in micro-scale interface evolution". In: *Mechanical Systems and Signal Processing* 139 (2020), p. 106615.

[3] N. N. Balaji. "Dissipative dynamics of bolted joints". Ph.D. Thesis. Houston, Texas: Rice University, 2021.

[4] R. M. Lacayo and M. S. Allen. “Updating structural models containing nonlinear Iwan joints using quasi-static modal analysis”. In: *Mechanical Systems and Signal Processing* 118 (2019), pp. 133–157. ISSN: 08883270.

[5] N. N. Balaji and M. R. W. Brake. “The surrogate system hypothesis for joint mechanics”. In: *Mechanical Systems and Signal Processing* 126 (2019), pp. 42–64. ISSN: 0888-3270.

[6] A. T. Mathis, N. N. Balaji, R. J. Kuether, A. R. Brink, M. R. W. Brake, and D. D. Quinn. “A review of damping models for structures with mechanical joints”. In: *Applied Mechanics Reviews* 72.4 (2020). ISSN: 0003-6900.

[7] J. H. Porter, N. N. Balaji, C. R. Little, and M. R. W. Brake. “A quantitative assessment of the model form error of friction models across different interface representations for jointed structures”. In: *Mechanical Systems and Signal Processing* 163 (2022), p. 108163. ISSN: 0888-3270.

[8] M. Krack, C. W. Schwingshackl, and M. R. W. Brake. “The tribomechadynamics research challenge”. In: *40th International Modal Analysis Conference (IMAC XL)*. Orlando, FL, 2022.

[9] J. A. Greenwood and J. B. P. Williamson. “Contact of nominally flat surfaces”. In: *Proceedings of the Royal Society of London. Series A. Mathematical and Physical Sciences* 295.1442 (1966). Publisher: Royal Society, pp. 300–319.

[10] A. A. Polycarpou and I. Etsion. “Analytical approximations in modeling contacting rough surfaces”. In: *Journal of Tribology* 121.2 (1999), pp. 234–239. ISSN: 0742-4787, 1528-8897.

[11] S. Björkland. “A random model for micro-slip between nominally flat surfaces”. In: *ASME Journal of Tribology* 119 (1997), pp. 726–732.

[12] M. Eriten, A. A. Polycarpou, and L. A. Bergman. “Physics-based modeling for fretting behavior of nominally flat rough surfaces”. In: *International Journal of Solids and Structures* 48.10 (2011), pp. 1436–1450. ISSN: 0020-7683.

[13] M. Eriten, A. A. Polycarpou, and L. A. Bergman. “Surface roughness effects on energy dissipation in fretting contact of nominally flat surfaces”. In: *Journal of Applied Mechanics* 78.2 (2011). Publisher: American Society of Mechanical Engineers Digital Collection. ISSN: 0021-8936.

[14] B. An, X. Wang, Y. Xu, and R. L. Jackson. “Deterministic elastic-plastic modelling of rough surface contact including spectral interpolation and comparison to theoretical models”. In: *Tribology International* 135 (2019), pp. 246–258. ISSN: 0301-679X.

[15] X. Wang, B. An, Y. Xu, and R. L. Jackson. “The effect of resolution on the deterministic finite element elastic-plastic rough surface contact under combined normal and tangential loading”. In: *Tribology International* 144 (2020), p. 106141. ISSN: 0301-679X.

[16] C. W. Schwingshackl, E. P. Petrov, and D. J. Ewins. “Measured and estimated friction interface parameters in a nonlinear dynamic analysis”. In: *Mechanical Systems and Signal Processing* 28 (2012), pp. 574–584.

[17] M. Lavella, D. Botto, and M. M. Gola. “Design of a high-precision, flat-on-flat fretting test apparatus with high temperature capability”. In: *Wear* 302 (2013), pp. 1073–1081.

[18] B. D. Yang and C. H. Menq. “Modeling of friction contact and its application to the design of shroud contact”. In: *Journal of Engineering for Gas Turbines and Power* 119.4 (1997), pp. 958–963.

[19] L. Pesaresi, J. Armand, C. W. Schwingshackl, L. Salles, and C. Wong. “An advanced underplatform damper modelling approach based on a microslip contact model”. In: *Journal of Sound and Vibration* (2018). ISSN: 0022-460X.

[20] C. Cattaneo. “Sul contatto di due corpi elastici: distribuzione locale degli sforzi”. In: *Rendiconti dell’Accademia Nazionale dei Lincei* 27 (1938), pp. 342–348, 434–436, 474–478.

[21] R. D. Mindlin. “Compliance of elastic bodies in contact”. In: *ASME Journal of Applied Mechanics* 16 (1949), pp. 259–268.

[22] R. D. Mindlin, W. P. Mason, T. F. Osmer, and H. Deresiewicz. “Effects of an oscillating tangential force on the contact surfaces of elastic spheres”. In: *Proceedings of the First National Congress of Applied Mechanics* (1951), pp. 203–208.

[23] R. D. Mindlin and H. Deresiewicz. “Elastic spheres in contact under varying oblique forces”. In: *ASME Journal of Applied Mechanics* 20 (1953), pp. 327–344.

[24] M. Eriten, A. A. Polycarpou, and L. A. Bergman. “Physics-based modeling for partial slip behavior of spherical contacts”. In: *International Journal of Solids and Structures* 47.18 (2010), pp. 2554–2567. ISSN: 0020-7683.

[25] W. Li, W. Zhan, and P. Huang. “A physics-based model of a dynamic tangential contact system of lap joints with non-Gaussian rough surfaces based on a new solution”. In: *AIP Advances* 10.3 (2020), p. 035207. ISSN: 2158-3226.

[26] W. Zhan and P. Huang. “Physics-based modeling for lap-type joints based on the Iwan model”. In: *Journal of Tribology* 140.5 (2018). Publisher: American Society of Mechanical Engineers Digital Collection. ISSN: 0742-4787.

[27] W. Zhan and P. Huang. “Modeling tangential contact based on non-Gaussian rough surfaces:” in: *Proceedings of the Institution of Mechanical Engineers, Part J: Journal of Engineering Tribology* (2018). Publisher: SAGE PublicationsSage UK: London, England.

[28] J. Chen, J. Zhang, J. Hong, and L. Zhu. “Modeling tangential contact of lap joints considering surface topography based on Iwan model”. In: *Tribology International* 137 (2019), pp. 66–75. ISSN: 0301-679X.

[29] H. Kang, Z.-M. Li, T. Liu, G. Zhao, J. Jing, and W. Yuan. “A novel multiscale model for contact behavior analysis of rough surfaces with the statistical approach”. In: *International Journal of Mechanical Sciences* 212 (2021), p. 106808. ISSN: 0020-7403.

[30] T. Dreher, M. R. W. Brake, B. Seeger, and M. Krack. “In situ, real-time measurements of contact pressure internal to jointed interfaces during dynamic excitation of an assembled structure”. In: *Mechanical Systems and Signal Processing* 160 (2021), p. 107859. ISSN: 0888-3270.

[31] M. Ruan. “The variability of strains in bolts and the effect on preload in jointed structure”. Masters Thesis. Houston, Texas: Rice University, 2019.

[32] Y.-R. Jeng and S.-R. Peng. “Elastic-plastic contact behavior considering asperity interactions for surfaces with various height distributions”. In: *Journal of Tribology* 128.2 (2006). Publisher: American Society of Mechanical Engineers Digital Collection, pp. 245–251. ISSN: 0742-4787.

[33] W. R. Chang, I. Etsion, and D. B. Bogy. “Static friction coefficient model for metallic rough surfaces”. In: *Journal of Tribology* 110.1 (1988), pp. 57–63. ISSN: 0742-4787, 1528-8897.

[34] A. W. Bush, R. D. Gibson, and G. P. Keogh. “Strongly anisotropic rough surfaces”. In: *Journal of Lubrication Technology* 101.1 (1979), pp. 15–20. ISSN: 0022-2305.

[35] J. Halling and K. A. Nuri. “Elastic/plastic contact of surfaces considering ellipsoidal asperities of work-hardening multi-phase materials”. In: *Tribology International* 24.5 (1991), pp. 311–319. ISSN: 0301-679X.

[36] J. H. Horng. “An elliptic elastic-plastic asperity microcontact model for rough surfaces”. In: *Journal of Tribology* 120.1 (1998), pp. 82–88. ISSN: 0742-4787.

[37] Y.-R. Jeng and P.-Y. Wang. “An elliptical microcontact model considering elastic, elastoplastic, and plastic deformation”. In: *Journal of Tribology* 125.2 (2003), pp. 232–240. ISSN: 0742-4787.

[38] N. N. Balaji, S. A. Smith, and M. R. W. Brake. “Evolution of the dynamics of jointed structures over prolonged testing”. In: *40th International Modal Analysis Conference (IMAC XL)*. Orlando, FL, 2022.

[39] H. Hertz. “Über die Berührung Fester Elastischer Körper (On the contact of elastic solids)”. In: *Journal fur die Reine und Andgewandte Mathematik* 92 (1882), pp. 156–171.

[40] K. L. Johnson. *Contact Mechanics.* Cambridge: Cambridge University Press, 1985.

[41] M. R. W. Brake. “Contact modeling across scales: from materials to structural dynamics applications.” In: *Journal of Structural Dynamics* (2021). ISSN: 2684-6500.

[42] H. Ghaednia, M. R. W. Brake, M. Berryhill, and R. L. Jackson. “Strain hardening from elastic–perfectly plastic to perfectly elastic flattening single asperity contact”. In: *Journal of Tribology* 141.3 (2019), p. 031402. ISSN: 0742-4787, 1528-8897.

[43] M. R. W. Brake. "An analytical elastic plastic contact model with strain hardening and frictional effects for normal and oblique impacts". In: *International Journal of Solids and Structures* 62 (2015), pp. 104–123.

[44] J. Jamari and D. J. Schipper. "An elastic–plastic contact model of ellipsoid bodies". In: *Tribology Letters* 21.3 (2006), pp. 262–271. ISSN: 1023-8883, 1573-2711.

[45] L. P. Lin and J. F. Lin. "An elliptical elastic-plastic microcontact model developed for an ellipsoid in contact with a smooth rigid flat". In: *Journal of Tribology* 129.4 (2007), pp. 772–782. ISSN: 0742-4787.

[46] Y. Wen, J. Tang, W. Zhou, and C. Zhu. "A new elliptical microcontact model considering elastoplastic deformation". In: *Proceedings of the Institution of Mechanical Engineers, Part J: Journal of Engineering Tribology* 232.11 (2018), pp. 1352–1364. ISSN: 1350-6501.

[47] R. Buczkowski and M. Kleiber. "Statistical models of rough surfaces for finite element 3D-contact analysi". In: *Archives of Computational Methods in Engineering* 16.4 (2009), pp. 399–424. ISSN: 1886-1784.

[48] L. Vu-Quoc, X. Zhang, and L. Lesburg. "A normal force-displacement model for contacting spheres accounting for plastic deformation: force-driven formulation". In: *ASME Journal of Applied Mechanics* 67 (2000), pp. 363–371.

[49] W.-R. Chang. "Contact, Adhesion, and Static Friction of Metallic Rough Surfaces". PhD thesis. Berkeley, California: University of California, Berkeley. 121 pp.

[50] R. L. Jackson and I. Green. "A finite element study of elasto-plastic hemispherical contact against a rigid flat". In: *ASME Journal of Tribology* 127 (2005), pp. 343–354.

[51] I. Etsion, Y. Kligerman, and Y. Kadin. "Unloading of an elastic-plastic loaded spherical contact". In: *International Journal of Solids and Structures* 42 (2005), pp. 3716–3729.

[52] H Deresiewicz. "Oblique contact of nonspherical elastic bodies". In: *Journal of Applied Mechanics* 24 (1957), pp. 623–624.

[53] N. Maw, J. R. Barber, and J. N. Fawcett. "The oblique impact of elastic spheres". In: *Wear* 38 (1976), pp. 101–114.

[54] W. C. Hurty. "Dynamic analysis of structural systems using component modes". In: *AIAA Journal* 3 (1960), pp. 678–685.

[55] R. R. Craig and M. C. C. Bampton. "Coupling of substructures for dynamic analyses". In: *AIAA Journal* 6.7 (1968), pp. 1313–1319.

[56] N. N. Balaji, T. Dreher, M. Krack, and M. R. W. Brake. "Reduced order modeling for the dynamics of jointed structures through hyper-reduced interface representation". In: *Mechanical Systems and Signal Processing* 149 (2021), p. 107249. ISSN: 0888-3270.

[57] A. Hielo. *RTBF Impact/Rebound Material Test.* Report SML0229. Sandia National Laboratories, 2012.

[58] S. Qu, C. X. Huang, Y. L. Gao, G. Yang, S. D. Wu, Q. S. Zang, and Z. F. Zhang. "Tensile and compressive properties of AISI 304L stainless steel subjected to equal channel angular pressing". In: *Materials Science and Engineering: A*. International Symposium on Inorganic Interfacial Engineering 2006 475.1 (2008), pp. 207–216. ISSN: 0921-5093.

[59] M. R. W. Brake, C. W. Schwingshackl, and P. Reuß. "Observations of variability and repeatability in jointed structures". In: *Mechanical Systems and Signal Processing* 129 (2019), pp. 282–307.

[60] M. Jin, W. Chen, M. R. W. Brake, and H. Song. "Identification of instantaneous frequency and damping from transient decay data". In: *Journal of Vibration and Acoustics* (2020), pp. 1–36.

[61] A. Akay. *Research Needs and Open Questions in Vibration Energy Transport and Dissipation.* Tech. rep. NSF Grant No: 0940347. National Science Foundation, 2016.

[62] S. Smith, J. C. Bilbao-Ludena, S. Catalfamo, M. R. W. Brake, P. Reuß, and C. W. Schwingshackl. "The effects of boundary conditions, measurement techniques, and excitation type on measurements of the properties of mechanical joints". In: *34th International Modal Analysis Conference (IMAC XXXIV).* Orlando, FL, 2016.

[63] M. R. Brake, P. Reuß, D. J. Segalman, and L. Gaul. "Variability and repeatability of jointed structures with frictional interfaces". In: *32nd International Modal Analysis Conference (IMAC XXXII).* Orlando, FL, 2014.

[64] S. A. Smith, M. R. W. Brake, and C. W. Schwingshackl. "On the characterization of nonlinearities in assembled structures". In: *Journal of Vibration Acoustics* 142.5 (2020). ISSN: 1048-9002.

[65] I. Amidror. "Scattered data interpolation methods for electronic imaging systems: a survey". In: *Journal of Electronic Imaging* 11.2 (2002). Publisher: International Society for Optics and Photonics, pp. 157–176. ISSN: 1017-9909, 1560-229X.

[66] W. Chen, M. Jin, I. Lawal, M. R. W. Brake, and H. Song. "Measurement of slip and separation in jointed structures with non-flat interfaces". In: *Mechanical Systems and Signal Processing* 134 (2019), p. 106325. ISSN: 0888-3270.

[67] M. Abramowitz and I. A. Stegun, eds. *Handbook of Mathematical Functions with Formulas, Graphs, and Mathematical Tables.* 5th. U.S. Government Printing Office, 1966.

[68] Y. Wen, J. Tang, W. Zhou, and L. Li. "A reconstruction and contact analysis method of three-dimensional rough surface based on ellipsoidal asperity". In: *Journal of Tribology* 142.041502 (2020). ISSN: 0742-4787.

[69] A. W. Bowman and A. Azzalini. *Applied Smoothing Techniques For Data Analysis.* Oxford University Press, 1997.

[70] N. N. Balaji and M. R. W. Brake. “A quasi-static non-linear modal analysis procedure extending Rayleigh quotient stationarity for non-conservative dynamical systems”. In: *Computers and Structures* 230 (2020), p. 106184. ISSN: 0045-7949.

[71] M. Krack. “Nonlinear modal analysis of nonconservative systems: extension of the periodic motion concept”. In: *Computers & Structures* 154 (2015), pp. 59–71. ISSN: 00457949.

[72] M. Krack, L. Salles, and F. Thouverez. “Vibration prediction of bladed disks coupled by friction joints”. In: *Archives of Computational Methods in Engineering* 24.3 (2017), pp. 589–636. ISSN: 1886-1784.

[73] J. J. Hollkamp and R. W. Gordon. “Reduced-order models for nonlinear response prediction: implicit condensation and expansion”. In: *Journal of Sound and Vibration* 318.4-5 (2008), pp. 1139–1153.

[74] H. Festjens, G. Chevallier, and J.-L. Dion. “A numerical tool for the design of assembled structures under dynamic loads”. In: *International Journal of Mechanical Sciences* 75 (2013), pp. 170–177.

[75] M. S. Allen, R. M. Lacayo, and M. R. W. Brake. “Quasi-static modal analysis based on implicit condensation for structures with nonlinear joints”. In: *International Conference on Noise and Vibration Engineering*. Leuven, Belgium, 2016.

[76] T. M. Cameron and J. H. Griffin. “An alternating frequency/time domain method for calculating the steady-state response of nonlinear dynamic systems”. In: *ASME Journal of Applied Mechanics* 56 (1989), pp. 149–154.

[77] J. Guillen and C. Pierre. “An Efficient, Hybrid, Frequency-Time Domain Method for The Dynamics of Large-Scale Dry-Friction Damped Structural Systems.” In: *IUTAM Symposium on Unilateral Multibody Contacts*. Ed. by F. Pfeiffer and C. Glocker. Solid Mechanics and Its Applications. Dordrecht: Springer Netherlands, 1999, pp. 169–178. ISBN: 978-94-011-4275-5.

[78] M. Krack and J. Groß. *Harmonic Balance for Nonlinear Vibration Problems*. Mathematical Engineering. Springer International Publishing, 2019. ISBN: 978-3-030-14022-9.

[79] A. Fantetti, L. R. Tamatam, M. Volvert, I. Lawal, L. Liu, L. Salles, M. R. W. Brake, C. W. Schwingshackl, and D. Nowell. “The impact of fretting wear on structural dynamics: experiment and simulation”. In: *Tribology International* 138 (2019), pp. 111–124.

[80] I. Etsion, O. Levinson, G. Halperin, and M. Varenberg. “Experimental investigation of the elastic–plastic contact area and static friction of a sphere on flat”. In: *Journal of Tribology* 127.1 (2005), pp. 47–50. ISSN: 0742-4787, 1528-8897.

[81] M. R. W. Brake. “Tutorial: tribomechadynamics and jointed structures”. In: *39th International Modal Analysis Conference (IMAC XXXIX)*. Virtual, 2021.

[82] M. R. Brake, D. J. Ewins, D. J. Segalman, L. A. Bergman, and D. D. Quinn. *Proceedings of the Fourth International Workshop on Jointed Structures*. Technical Report SAND2016-9962. Sandia National Laboratories, Albuquerque, NM, 2016.

[83] J. H. Porter. *Microslip Rough Contact*. URL: `https://github.com/tmd-lab/microslip-rough-contact`.